Politecnico di Torino

Master's Degree in Aerospace Engineering

Master's Thesis

Development of a multibody analysis methodology for transmission systems

Supervisors:

Prof. Teresa Maria Berruti
Prof. Stefano Zucca
Eng. Davide Allaio
Eng. Marco Tommasi

Candidate:

Riccardo Villani

Graduation Session: July 2026

Abstract

This thesis builds on a previous work in which an *MSC Adams* model of a reduction gearbox for a turboprop engine developed by *Avio Aero* was created using the *Gear AT* tool, with all components represented as flexible bodies. While the previous study investigated the *slow-roll regime*, the present work focuses on the behavior of the model at higher rotational speeds in order to assess the performance of *MSC Adams* in high-speed dynamic simulations involving flexible-body interactions and high-frequency phenomena.

The study investigates the influence of initial conditions, *speed-sweep* direction, simulation-time *partitioning*, and selected model parameters on the numerical response. Two speed-sweep approaches are compared to evaluate the effects of transient behavior and numerical artifacts appearing as vertical banding in the *Campbell diagrams*. The results show that sweep-down analyses are more affected by these artifacts, while finer time partitioning reduces their presence.

A quantitative assessment of the numerical results is then carried out through comparisons between simulated and theoretical kinematic and dynamic quantities. These comparisons indicate that the results can be considered sufficiently accurate, despite nonzero offsets and increasing noise in higher-order derivatives. The analysis also highlights the limitations of the *HHT-I3* solver and suggests that symmetry is preserved in the mean response, but not fully in the dynamic component.

Finally, a *modal analysis* is performed, highlighting an oscillatory pattern in the computed eigenvalues and the influence of rotational speed, resisting torque, and reference marker selection.

Contents

List of Figures

List of Tables

Chapter 1

Introduction

1.1 Previous work

The present thesis builds on the work presented in [1], which established the multibody modeling framework adopted in this study. Because *MSC Adams* had not previously been used within the company for this type of application, the earlier thesis included an initial development phase based on a simple rotor with multiple degrees of freedom, aimed at gaining familiarity with the *Gear AT* tool and its modeling methodology. The reduction gearbox was then modeled in successive stages with increasing levels of fidelity: first as a rigid-body system, then with flexible gear teeth only, and finally as a fully flexible assembly.

The resulting model was subsequently examined under slow-roll operating conditions, including the assessment of tooth microgeometry modifications. In this way, the previous work laid the groundwork for the investigation of high-frequency dynamic effects in aeronautical transmission systems. The present thesis continues this line of research by extending the analysis to higher rotational speeds.

1.2 Thesis objectives

The present thesis continues the line of research initiated in the previous work, with the broader aim of evaluating the capability of a commercial software tool to perform analyses relevant to industrial applications in the field of gearbox dynamics. While the earlier thesis focused on the development of the model and its behavior under slow-roll operating conditions, the present work extends the investigation to higher-speed dynamic simulations characterized by flexible-component interactions and high-frequency phenomena.

Particular attention is devoted to evaluating the influence of selected analysis parameters on the numerical response at high rotational speeds, since full speed-sweep analyses require a sensitivity assessment to determine how specific parameters affect the computed results and how they should be properly selected.

In addition, the possibility of performing a modal analysis of the entire assembly is explored in order to identify the natural frequencies of the system and compare them with the peaks observed in the dynamic response.

The remainder of this thesis is organized as follows. After an initial chapter introducing the theoretical background, the next chapter presents the main numerical investigations, focusing on the influence of initial conditions, speed-sweep direction,

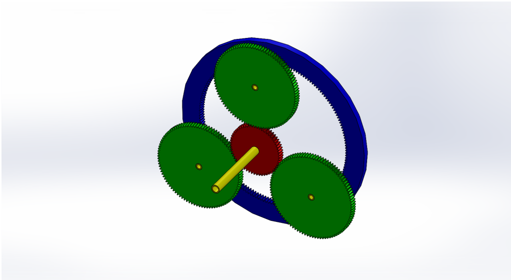

(a) Isometric view of the gearbox model.

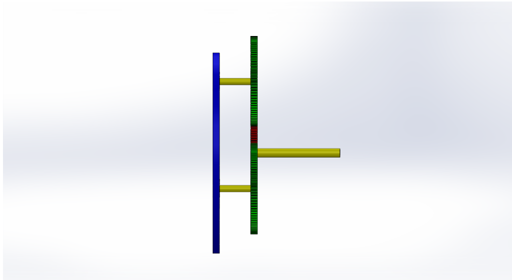

(b) Side view of the gearbox model.

Figure 1.1: Schematic representation of the *MSC Adams* model used in this thesis. For confidentiality reasons, the geometry shown differs from the actual model while preserving its overall layout and functional architecture.

and time-interval partitioning on the simulation results. This is followed by a chapter devoted to the validation of the numerical results through the comparison of selected kinematic and dynamic quantities. A subsequent chapter then addresses the modal analysis procedure and the corresponding eigenvalue trends.

1.3 Model description

The model adopted in this work is derived from a real component, namely the reduction gearbox of a turboprop engine developed by *Avio Aero*. A schematic representation of this system is shown in Figure 1.1.

The representation is included solely to illustrate the model structure; for confidentiality reasons, the geometry shown differs from the model used in the simulations. The gearbox consists of two reduction stages that reduce the rotational speed from the turbine to the propeller.

The input shaft, connected to the turbine, transmits motion to the entire system. The sun gear, located at its end, meshes with three large planet gears in a planetary arrangement, thereby forming the first reduction stage. Each large planet gear is mounted on a layshaft, which also carries a small planet gear rotating at the same angular speed. The three small planet gears mesh with the ring gear, thereby completing the second reduction stage, while the output shaft connected to the ring gear transmits motion to the propeller.

The various components were modeled using the *Gear AT* tool within *MSC Adams*, which allows the gear generation parameters to be specified, including tooth microgeometry modifications. All components were modeled as flexible bodies and, through the *multi-gear-shaft* option, multiple flexible gears can be placed on the same flexible shaft. As a compromise between accuracy and computational cost, the mesh is finer in the tooth region than in the gear body, and the two discretizations are connected through a glued contact.

The interactions between the gear elements are defined through the so-called *Gear AT Force* feature, each instance of which models the contact between a pair of meshing gears by computing the exchanged forces and torques, while also accounting for structural and lubrication damping. Further details can be found in the *Gear AT > Gear AT Force > New Gear AT Force* section of the Adams Machinery User Guide [2].

Chapter 2

Theoretical Background

This chapter provides a brief theoretical background on the main topics relevant to this work. In particular, it addresses multibody systems, time integration in nonlinear dynamics, and the HHT method.

2.1 Multibody Systems

This section presents a brief overview of multibody systems. A more detailed discussion can be found in [3], which provides the basis for the concepts discussed in this section, as well as for the related figures.

A multibody system can be defined as a collection of subsystems, referred to as bodies, components, or substructures. Their motion is constrained by means of different types of joints, and each subsystem may undergo large translational and rotational displacements. Figure 2.1 shows a schematic representation of a multibody system.

Three theoretical frameworks can be identified when describing body motion: rigid-body mechanics, structural mechanics, and continuum mechanics.

For a rigid body, the distance between any two points remains constant over time, and the motion of the entire body can be completely described using six generalized coordinates. In structural mechanics, deformation is taken into account, whereas large rigid-body rotations are typically not considered. As a result, a large num-

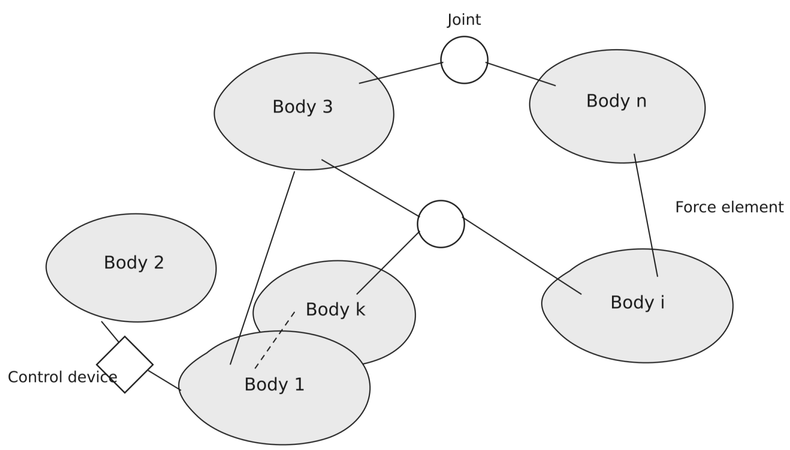

Figure 2.1: Schematic representation of a multibody system.

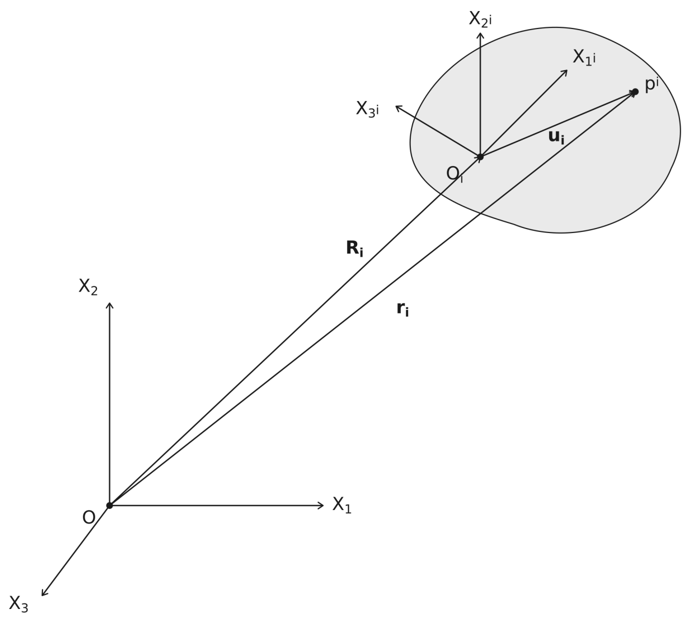

Figure 2.2: Schematic representation of rigid-body kinematics.

ber of elastic coordinates may be required to describe the deformation accurately. Continuum mechanics provides a more general framework in which both rigid-body motion and deformation can be represented, leading to mathematical models characterized by high nonlinearity and large dimensionality.

2.1.1 Rigid Body Kinematics

Rigid bodies are characterized by a distributed mass and by a constant distance between any two points of the body. Because of this, the motion of a rigid body in space can be described using only six generalized coordinates: three associated with translation and three with orientation.

Figure 2.2 shows the kinematic description of a rigid body in three-dimensional space. $\mathbf{X}_1$, $\mathbf{X}_2$, and $\mathbf{X}_3$ denote the inertial reference frame, while $\mathbf{X}_1^i$, $\mathbf{X}_2^i$, and $\mathbf{X}_3^i$ denote the body-fixed reference frame, whose origin is located at point O^i.

For a rigid body, the position of an arbitrary point P^i can be expressed as the sum of the position vector of the origin O^i of the body-fixed reference frame and the local position vector of the point with respect to that origin, that is

$$\mathbf{r}^i = \mathbf{R}^i + \mathbf{u}^i \tag{2.1}$$

where $\mathbf{r}^i$ is the global position vector of point P^i, $\mathbf{R}^i$ is the global position vector of the origin O^i, and $\mathbf{u}^i$ is the position vector of P^i with respect to O^i. Since the body is rigid, the local vector $\mathbf{u}^i$ remains constant over time.

By differentiating the position vector with respect to time, the velocity of point P^i is obtained as

$$\mathbf{v}^i = \dot{\mathbf{R}}^i + \boldsymbol{\omega}^i \times \mathbf{u}^i \tag{2.2}$$

where $\dot{\mathbf{R}}^i$ is the translational velocity of the origin O^i and $\boldsymbol{\omega}^i$ is the angular velocity of the body. The velocity of a generic point on a rigid body is therefore composed of a translational contribution and a rotational contribution.

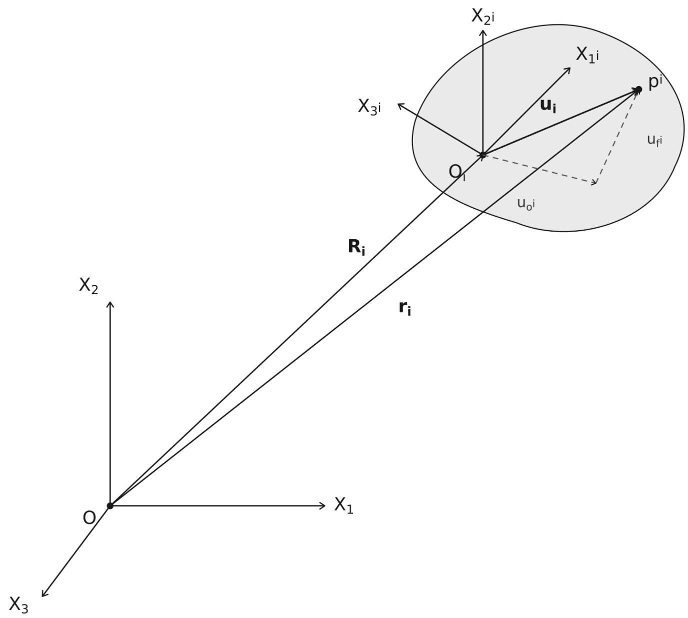

Figure 2.3: Schematic representation of deformable-body kinematics.

By differentiating once more, the acceleration of point P^i can be written as

$$\mathbf{a}^i = \ddot{\mathbf{R}}^i + \boldsymbol{\alpha}^i \times \mathbf{u}^i + \boldsymbol{\omega}^i \times \left(\boldsymbol{\omega}^i \times \mathbf{u}^i\right) \tag{2.3}$$

Thus, the acceleration includes a translational term, a tangential term associated with angular acceleration, and a centripetal term associated with angular velocity.

2.1.2 Deformable-Body Kinematics

In the deformable-body formulation, the kinematic description of an arbitrary point is more complex than in the rigid-body case. As shown in Figure 2.3, the position of a generic point P^i depends not only on the motion of the body reference frame, but also on the deformation of the body with respect to that frame.

As in the rigid-body case, an inertial reference frame and a body-fixed reference frame are introduced. However, in the deformable-body formulation, the position of point P^i is no longer described solely by a constant local vector, but also by an additional deformation vector $\mathbf{u}_f^i$.

The position vector of point P^i can be written as

$$\mathbf{r}^i = \mathbf{R}^i + \mathbf{u}_0^i + \mathbf{u}_f^i \tag{2.4}$$

where $\mathbf{R}^i$ is the position vector of the origin O^i of the body-fixed reference frame, $\mathbf{u}_0^i$ is the local position vector of the point in the undeformed configuration, and $\mathbf{u}_f^i$ is the additional displacement due to deformation. Unlike the rigid-body case, the local position vector of the point is therefore no longer constant over time.

By differentiating the position vector with respect to time, the velocity of point P^i is obtained as

$$\mathbf{v}^i = \dot{\mathbf{R}}^i + \boldsymbol{\omega}^i \times \left(\mathbf{u}_0^i + \mathbf{u}_f^i\right) + \left(\dot{\mathbf{u}}_f^i\right)_r \tag{2.5}$$

where $\dot{\mathbf{R}}^i$ is the translational velocity of the body reference frame, $\boldsymbol{\omega}^i$ is the angular velocity of the body, and $\left(\dot{\mathbf{u}}_f^i\right)_r$ is the time derivative of the deformation vector evaluated in the rotating reference frame.

By differentiating once more, the acceleration of point P^i can be expressed as

$$\mathbf{a}^i = \ddot{\mathbf{R}}^i + \dot{\boldsymbol{\omega}}^i \times \mathbf{u}^i + \boldsymbol{\omega}^i \times \left(\boldsymbol{\omega}^i \times \mathbf{u}^i\right) + 2\boldsymbol{\omega}^i \times \left(\dot{\mathbf{u}}^i_f\right)_r + \left(\ddot{\mathbf{u}}^i_f\right)_r \tag{2.6}$$

with

$$\mathbf{u}^i = \mathbf{u}^i_0 + \mathbf{u}^i_f \tag{2.7}$$

Compared with the rigid-body formulation, the expressions for velocity and acceleration include additional terms associated with the deformation field and its time derivatives. As a result, deformable-body models require a larger number of degrees of freedom and lead to a more computationally demanding formulation. In principle, a continuous deformable body would require an infinite number of equations to describe the motion of all its points. In practice, this difficulty is addressed by introducing approximate formulations, such as Rayleigh–Ritz approaches or, more commonly, the finite element method.

2.1.3 Constraints in Multibody Systems

In multibody systems, the motion of the bodies is generally restricted by constraints arising from mechanical joints or prescribed trajectories. These constraints reduce the mobility of the system, since the motion of the individual bodies is no longer independent. For a spatial system composed of n_b rigid bodies and subject to n_c independent constraint equations, the number of degrees of freedom m can be expressed as

$$m = 6n_b - n_c \tag{2.8}$$

This relation shows that the kinematic behavior of the system depends not only on the number of bodies involved, but also on the number of constraints imposed on them. In general, such constraints are described by nonlinear algebraic equations, which must be satisfied throughout the motion and thus play a fundamental role in the kinematic and dynamic formulation of multibody systems.

2.2 Time integration in Nonlinear Dynamics

This section provides a brief overview of time integration in nonlinear dynamics. The discussion is mainly based on [4], to which the reader is referred for a more comprehensive treatment.

In the analysis of multibody systems, the dynamic response is often governed by nonlinear relationships arising from large rigid-body rotations, body deformation, and kinematic constraints. Because of these sources of nonlinearity, closed-form analytical solutions are generally not available, especially in forward dynamics problems, where the objective is to determine the motion of the system under assigned external forces. For this reason, the system response is typically obtained by means of numerical time integration, which allows the position, velocity, and acceleration of the bodies to be evaluated over the time interval of interest.

In general, the equations of motion can be reformulated in state-space form, so that the original second-order problem is expressed as a system of first-order differential equations of the form

$$\dot{\mathbf{y}} = \mathbf{f}(\mathbf{y}, t) \tag{2.9}$$

where $\mathbf{y}$ is the state vector collecting the independent coordinates and their first time derivatives. The numerical solution is then advanced incrementally in time, starting from known initial conditions and updating the system state at each time step. Although simple integration schemes are available, engineering applications usually require more accurate and robust methods to ensure a reliable representation of the dynamic response.

A suitable time integration scheme for nonlinear dynamics must provide a satisfactory balance between accuracy, stability, and computational efficiency. This aspect is particularly important in complex multibody systems, where nonlinear effects, flexible components, and kinematic constraints may significantly increase the numerical sensitivity of the problem. In constrained systems, moreover, the integration algorithm must handle the coupled differential and algebraic equations consistently, so as to avoid the progressive accumulation of numerical errors and the consequent violation of the imposed constraints.

Another important issue is the treatment of the high-frequency content of the response. In many integration schemes, numerical errors become more significant as the frequency increases, leading to a deterioration of the computed solution. In complex models, this may result in spurious high-frequency oscillations of numerical origin, which do not correspond to the actual physical behavior of the system but may still compromise the stability and efficiency of the simulation.

For these reasons, robust integration schemes with controlled numerical dissipation are of particular interest in nonlinear dynamics. Among them, the Hilber-Hughes-Taylor (HHT) method is especially relevant, since it introduces numerical damping capable of attenuating non-physical high-frequency oscillations while preserving the accuracy of the lower-frequency response. The main features of this method are discussed in the following section.

2.3 HHT Method

This section provides a brief overview of the Hilber-Hughes-Taylor (HHT) method. The discussion is based on the original formulation proposed in [5], as well as on its implementation in the Adams Solver User's Guide [6].

The Hilber-Hughes-Taylor (HHT) method, often referred to as the α-method, is a family of one-step integration algorithms developed for the direct integration of the equations of motion in structural dynamics. Introduced in 1977, the method was proposed to overcome some of the limitations of previously adopted schemes, such as the Newmark, Wilson, and Houbolt methods, particularly with regard to the treatment of numerical dissipation. In many engineering applications, the physically relevant response is mainly associated with the lower-frequency modes of the system, whereas the high-frequency content may be strongly influenced by numerical artifacts introduced by the spatial discretization. For this reason, the possibility of introducing controlled numerical dissipation is particularly important.

The main idea of the HHT method is to provide numerical damping that acts primarily on the high-frequency portion of the response, while preserving the accuracy of the lower-frequency modes. This is achieved through the introduction of an additional parameter, α, which modifies the discrete equations of motion while retaining the standard Newmark relations for displacement and velocity. In this way, the method is able to attenuate spurious high-frequency oscillations without significantly altering the dynamic response of primary interest. From a numerical point of view, one of the main advantages of the HHT method is that it allows the amount of dissipation to be controlled continuously through a single parameter, while remaining unconditionally stable for linear problems.

Within the *MSC Adams* environment, the HHT method is implemented in the C++ solver as a stiff integration scheme for complex multibody dynamics. In contrast to backward-difference formulations such as GSTIFF, the HHT solver can be interpreted numerically as a low-pass filter, since it suppresses high-frequency oscillations while preserving the lower-frequency response with good accuracy. This feature is particularly relevant in simulations involving flexible bodies, contacts, and other sources of local dynamic stiffness, where the high-frequency content may be dominated by numerical noise rather than by physically meaningful behavior.

The control of numerical dissipation in the *MSC Adams* implementation is governed by the parameter α. Lower values of this parameter, typically approaching -0.3, reduce the cut-off frequency and therefore lead to a more aggressive filtering of high-frequency numerical noise. Although the HHT method is of lower order and may require smaller time steps to maintain accuracy, it generally provides more moderate and better distributed numerical damping than GSTIFF, and may produce less smooth acceleration and reaction-force histories. In addition, it may require fewer Jacobian evaluations, thereby improving computational efficiency in complex simulations.

In the present work, the HHT solver is used in the Index-3 formulation, corresponding to the setting *Integrator = 3*. This formulation enforces the kinematic position constraints rigorously and monitors the integration error on the basis of the system displacements only, without directly including the velocities in the error estimate. As a result, the solver is particularly fast and robust for models characterized by a wide frequency spectrum.

For the type of simulations considered in this thesis, involving flexible-body interactions and high-frequency dynamic phenomena, the HHT method in its Index-3 formulation is therefore especially suitable. In such systems, the high-frequency response is often associated with numerical artifacts or strongly damped local modes that do not contribute significantly to the global dynamic behavior. The low-pass filtering effect of the HHT solver helps stabilize the simulation and improve convergence, while preserving satisfactory accuracy in the global displacement response of the system.

Chapter 3

Influence of Analysis Parameters on Simulation Results

In the context of dynamic simulations, it is essential to understand how the main analysis parameters influence the computed response and how they should be selected in order to obtain reliable results. In the present work, this aspect is particularly important because the objective is to perform a full speed-sweep of the gearbox model under high-speed operating conditions. Preliminary analyses showed that some analysis parameters can significantly affect the results and may also influence the occurrence of vertical banding in the Campbell diagrams. For this reason, this chapter investigates the sensitivity of the simulation results to a selected set of analysis parameters.

More specifically, this chapter examines the influence of three aspects: initial conditions, speed-sweep direction, and time-interval partitioning.

The different analyses are compared using Campbell diagrams and frequency-content plots of the main excitation sources. These include the rotational frequencies of the main rotating components, expressed in Hertz, together with the *gear meshing frequency* (GMF), which, for simple and epicyclic gear trains in STAR configuration, is defined as

$$GMF = N \cdot Z$$

where N is the rotational speed of the gear, expressed in Hertz, and Z is the number of teeth. The gear meshing frequency represents the vibration excitation associated with the periodic engagement of the gear teeth.

In the following, GMF_1 and GMF_2 denote the gear meshing frequencies of the first and second reduction stages, respectively, while N_{in}, N_{planet}, and N_{out} denote the rotational frequencies of the input shaft, the planet gears, and the output shaft.

In addition to the fundamental excitation frequencies, selected harmonics are also considered. In particular, harmonics up to $4 \times GMF$ are monitored for the gear meshing frequency, whereas harmonics up to $3 \times N$ are considered for the rotational-frequency contributions, since they are sufficient to describe the main phenomena observed in this model.

Each Campbell diagram is accompanied by the corresponding peak-hold spectrum and overall response. To ensure consistency in the comparison of the different analyses, all Campbell diagrams are generated from the same raw signal. In the present work, this signal is defined as the total tooth-contact force exchanged by the teeth of the large planet 2 gear with the sun gear. More specifically, *MSC Adams* provides the force associated with each individual tooth in contact, and these contributions are summed to obtain the overall force exchanged by the large planet 2 gear teeth. This signal is then used to generate the Campbell diagrams throughout the chapter.

In the present chapter, for confidentiality reasons, all reported frequency-content plots show amplitudes normalized with respect to the maximum value of $2 \times GMF_2$. In addition, in all other plots, numerical values have been removed from the axes, with the exception of the simulation-time axis where relevant.

3.1 Effects of initial conditions

The aim of this section is to assess how the choice of initial conditions affects the simulation results. More specifically, it investigates whether a complete speed-sweep can be divided into multiple shorter runs without introducing significant differences in the response. This strategy may reduce the overall computational time by taking advantage of parallel simulations. In *MSC Adams*, two simulations can in fact be run simultaneously.

In the present analyses, the rigid-body initial angular velocity is the only initial condition that differs between the two cases, whereas the initial conditions associated with the flexible states are not directly prescribed and are assumed null throughout this section.

To evaluate the effect of this approach, two analyses are compared. Both are speed-sweep simulations performed with the same constant angular acceleration. All analysis parameters are kept identical, except for the rigid-body initial angular velocity and the simulation duration.

The two analyses differ as follows:

1. the first simulation starts from standstill, with zero rigid-body initial angular velocity, and covers a longer time interval;

2. the second simulation starts from the speed reached after 16 seconds in the first simulation and therefore uses a nonzero rigid-body initial angular velocity. Consequently, it is performed over a shorter time interval.

3.1.1 Baseline simulation: start-up from standstill

This baseline analysis consists of a speed-sweep performed with constant angular acceleration. The simulation starts from standstill, and the model is accelerated for approximately 43 seconds. Throughout this chapter, this case is referred to as *Long - Zero-Speed Start*.

Figure 3.1a shows the Campbell diagram obtained for this analysis, together with the corresponding peak-hold spectrum and overall response. For comparison with the second analysis, only the relevant speed range is reported; the full simulation range is therefore not shown. Two vertical bands are visible in the colormap. These features are associated with localized peaks in the response, as can also be observed in the raw signal shown in Figure 3.1b.

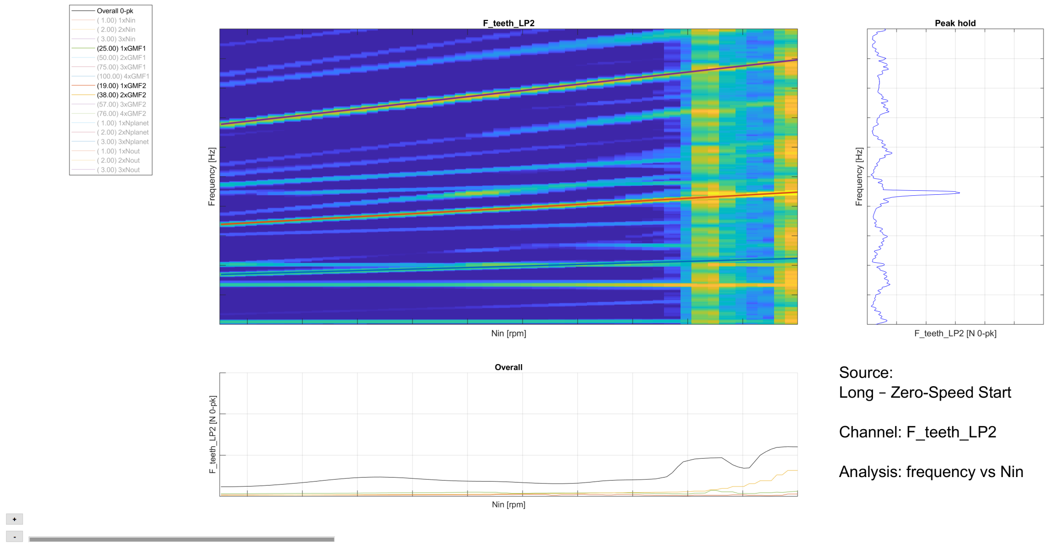

(a) Campbell diagram

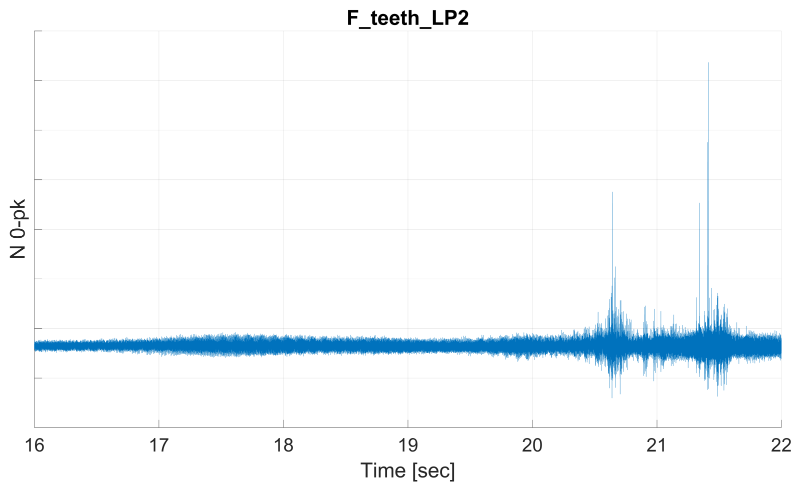

(b) Raw signal

Figure 3.1: Extended Campbell diagram, including peak-hold spectrum and overall response, together with the raw signal of the total tooth-contact force of the large planet 2 gear for the *Long - Zero-Speed Start* analysis.

3.1.2 Restarted simulation: short time window from a predefined operating point

The setup of this second analysis was defined a posteriori on the basis of the results obtained from the *Long - Zero-Speed Start* case. After examining the corresponding Campbell diagram, the vertical bands observed in the response were identified, and a sufficiently clean region around 16 seconds was selected as the restart point. This choice was made to avoid having the phenomenon of interest occur at the very beginning of the simulation.

The duration of the short analysis was then chosen so that the simulation would extend slightly beyond the speed at which the first vertical band appears in the *Long - Zero-Speed Start* case. In this way, the same speed region could be analyzed in both cases in order to assess whether the phenomenon would appear again. Throughout this chapter, this case is referred to as *Short - Nonzero-Speed Start*.

Figure 3.2a shows the Campbell diagram obtained for this analysis, together with the corresponding peak-hold spectrum and overall response. Unlike in the previous analysis, no vertical bands are observed at the end of the simulation, whereas one is visible near its beginning. This feature is also associated with a peak in the raw signal shown in Figure 3.2b.

3.1.3 Discussion of differences

The two simulations exhibit some common features, such as the crossing of a system mode excited by the $2 \times GMF_2$ contribution. Despite this, differences are observed at both the beginning and the end of the speed range considered for the comparison. A first indication of these differences can already be seen in the raw signals shown in Figure 3.3, where high peaks appear in different regions of the two responses.

The frequency-content plots of the main excitation sources shown in Figure 3.4 also highlight two main differences between the excitation-frequency trends of the two analyses. The first affects the low-speed region and is associated with the initial transient response of the *Short - Nonzero-Speed Start* analysis, which decays after approximately one second. No corresponding transient is present in the same speed range in the *Long - Zero-Speed Start* analysis, since by 16 seconds the initial transient has already ended. The second difference concerns the higher-speed region, where the *Long - Zero-Speed Start* analysis is affected by vertical banding. This phenomenon is not observed in the *Short - Nonzero-Speed Start* analysis and leads to discrepancies between the results of the two simulations.

Despite these differences, the shorter simulation appears to provide more physically consistent results than the longer one, which exhibits vertical banding even after the end of the initial transient, together with noise and spurious peaks. From a practical point of view, this suggests that a full speed-sweep of the system should preferably be split into multiple shorter sweeps. In this context, the first second of each simulation should be excluded from the comparison, as it is affected by the initial transient; this convention is implicitly adopted in the subsequent analyses discussed in this thesis. The improved behavior of the shorter simulations may instead be related to the reduced accumulation of integration errors, which in long-duration analyses may contribute to vertical banding, spurious peaks, and noise.

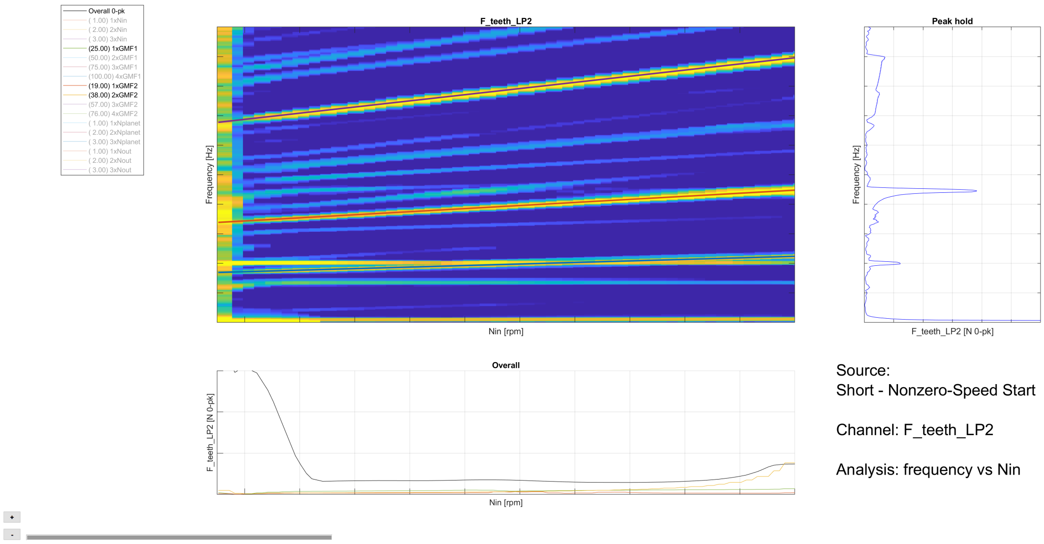

(a) Extended Campbell diagram

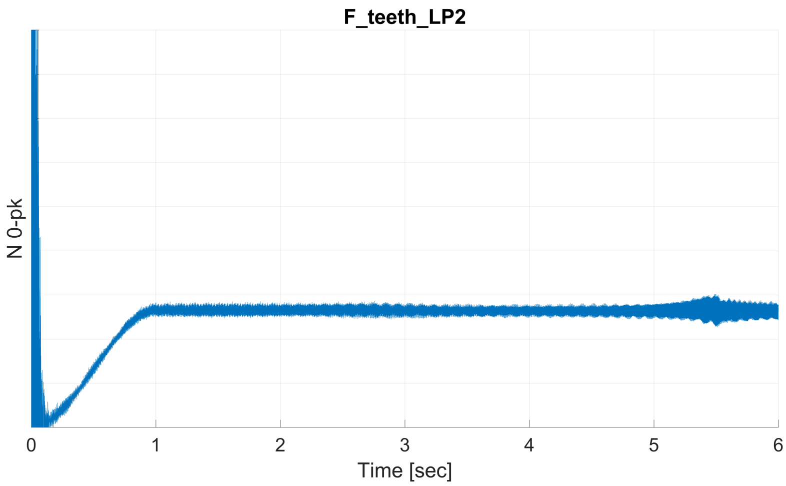

(b) Raw signal

Figure 3.2: Extended Campbell diagram, including peak-hold spectrum and overall response, together with the raw signal of the total tooth-contact force of the large planet 2 gear for the *Short - Nonzero-Speed Start* analysis.

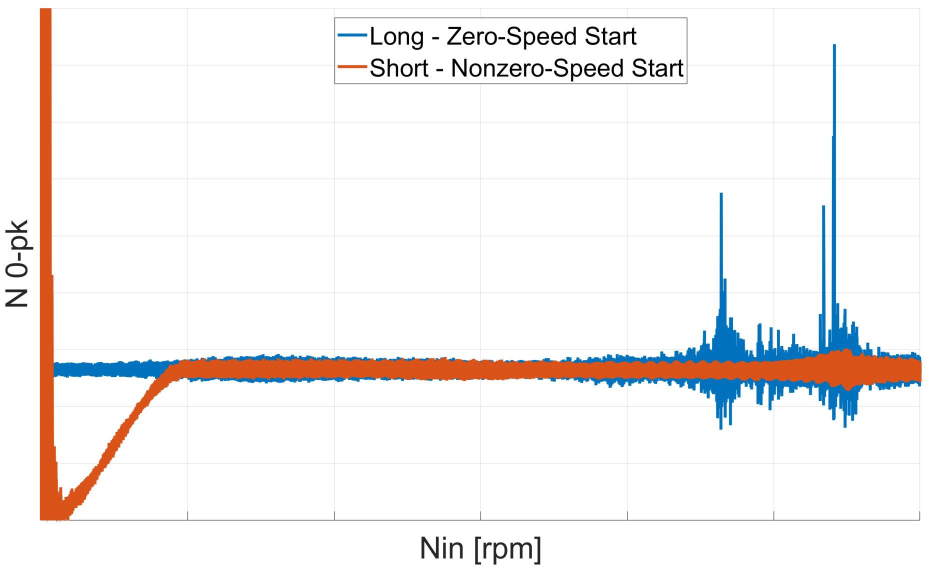

Figure 3.3: Comparison of the raw signals of the total tooth-contact force of the large planet 2 gear for the *Long - Zero-Speed Start* and *Short - Nonzero-Speed Start* analyses.

GMF_1 harmonics

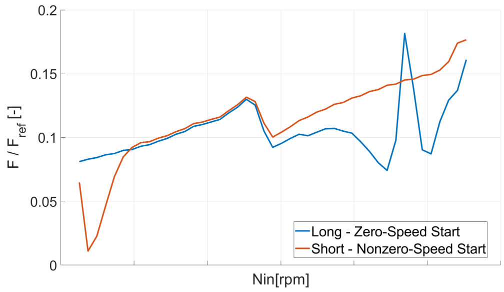

(a) $1 \times GMF_1$

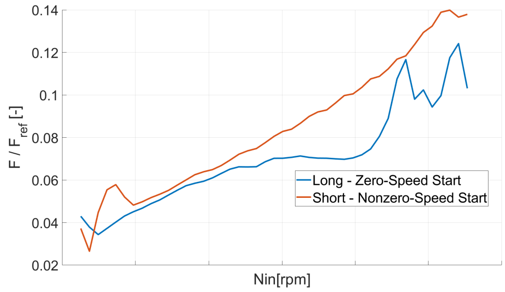

(b) $2 \times GMF_1$

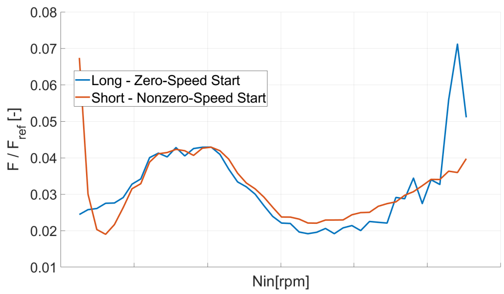

(c) $3 \times GMF_1$

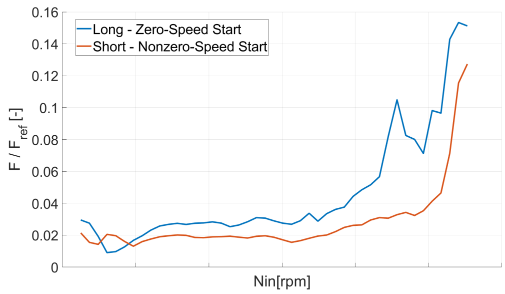

(d) $4 \times GMF_1$

GMF_2 harmonics

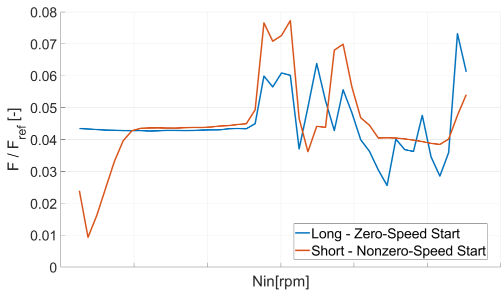

(e) $1 \times GMF_2$

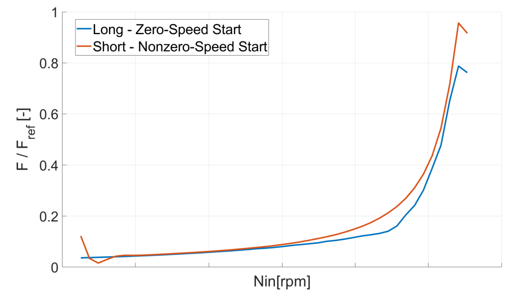

(f) $2 \times GMF_2$

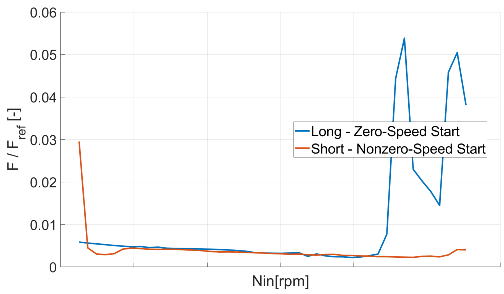

(g) $3 \times GMF_2$

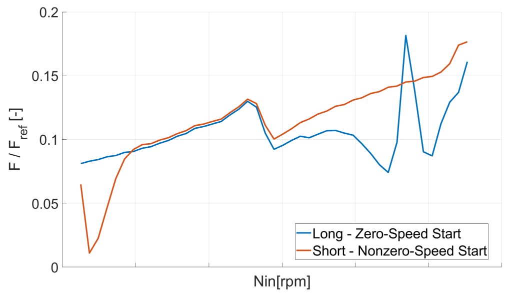

(h) $4 \times GMF_2$

Figure 3.4: Comparison of the main harmonic contributions for the *Long - Zero-Speed Start* and *Short - Nonzero-Speed Start* analyses, including the first four harmonics of GMF_1 and GMF_2, and the first three harmonics of N_{in}, N_{planet}, and N_{out}.

N_{in} harmonics

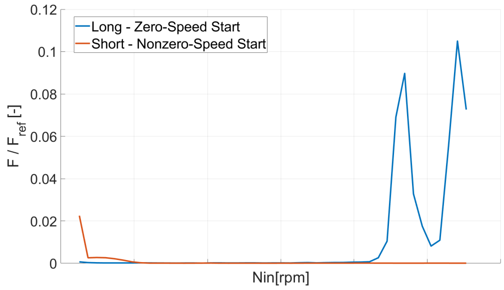

(i) $1 \times N_{in}$

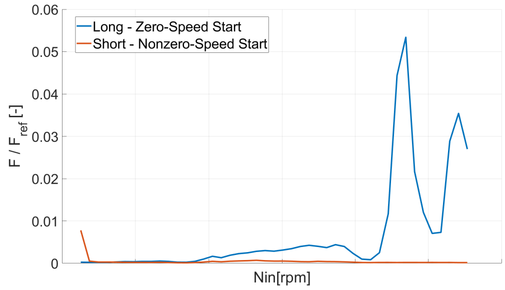

(j) $2 \times N_{in}$

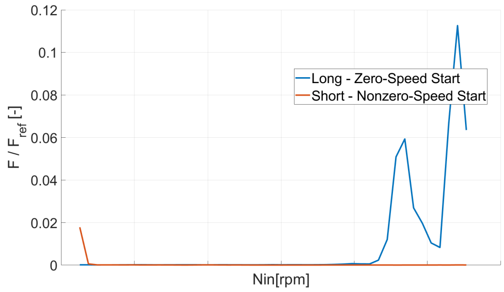

(k) $3 \times N_{in}$

N_{planet} harmonics

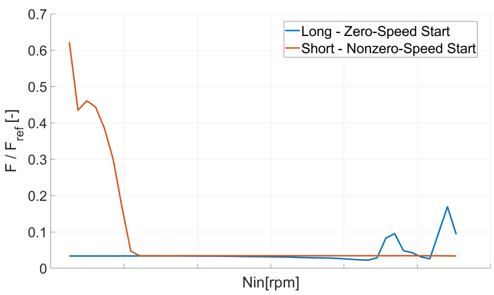

(l) $1 \times N_{planet}$

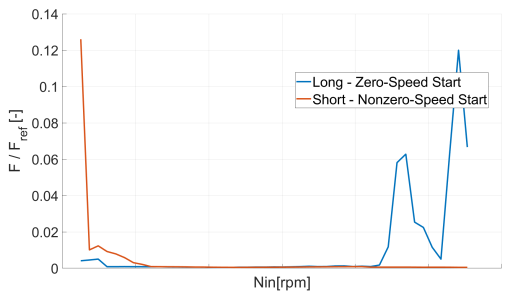

(m) $2 \times N_{planet}$

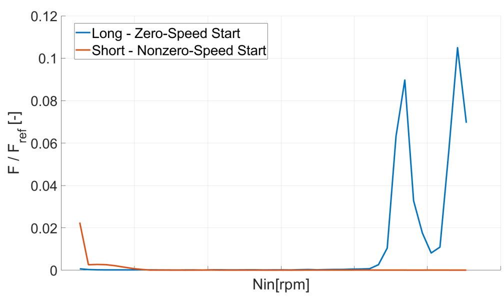

(n) $3 \times N_{planet}$

Figure 3.4: Comparison of the main harmonic contributions for the two initial-condition analyses (continued).

N_{out} harmonics

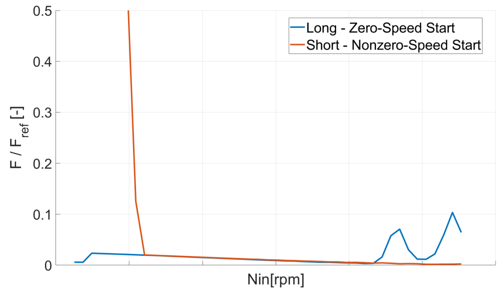

(o) $1 \times N_{out}$

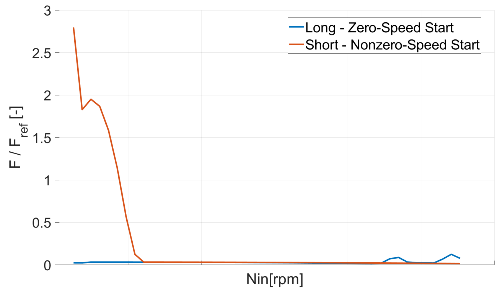

(p) $2 \times N_{out}$

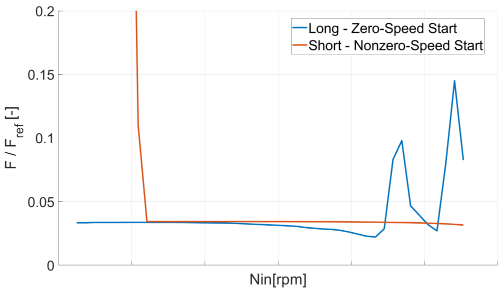

(q) $3 \times N_{out}$

Figure 3.4: Comparison of the main harmonic contributions for the two initial-condition analyses (continued).

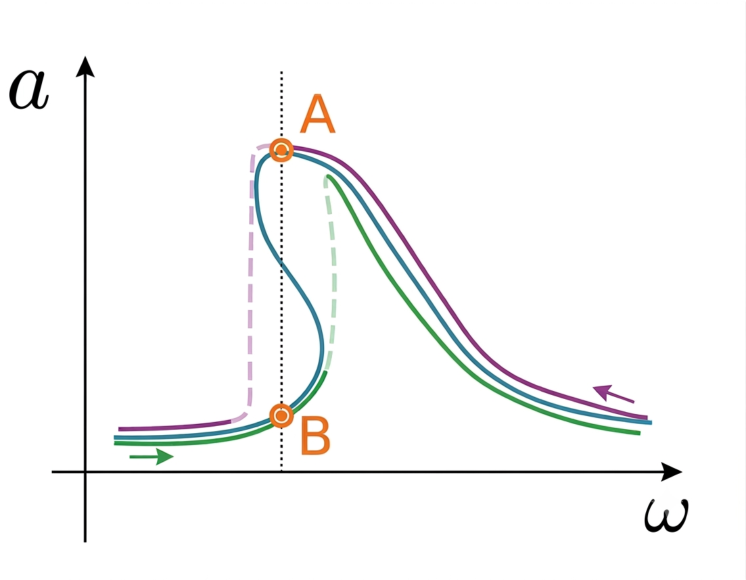

Figure 3.5: Schematic representation of jump phenomena in a nonlinear system with coexisting stable steady-state solutions.

3.2 Effect of speed-sweep direction

This section investigates the influence of the speed-sweep direction on the computed results. The main objective is to assess whether reversing the sweep direction affects the occurrence and intensity of the vertical bands observed in long-duration analyses. More generally, the analysis aims to evaluate how the sweep direction influences the system response.

In nonlinear systems with intermittent contact phenomena, such as geared transmissions with backlash, the steady-state response may not be uniquely defined over the entire speed range covered by the sweep. In particular, within specific speed intervals, multiple stable solutions may coexist. This means that, at the same rotational speed, the system may vibrate in different states depending on the path followed to reach that operating condition. As a consequence, during an upward or downward speed-sweep, the response may follow different branches, leading to hysteresis-like behavior and possible *jump phenomena* [7].

A schematic representation of this behavior is shown in Figure 3.5. In the coexistence region, the system may follow one stable branch during an upward sweep and a different response path during a downward sweep. As a result, the same excitation frequency may be associated with two different response amplitudes, here denoted as states A and B. This type of behavior therefore provides a possible framework for interpreting sweep-direction-dependent differences in the response.

To investigate this aspect, two types of analyses are considered, and the effect of the speed-sweep direction is examined both through comparisons across different analyses and within a single simulation:

1. *SWP - Monotonic Speed-Sweep*: analyses performed with constant angular acceleration, either positive or negative;

2. *CYC - Cyclic Speed-Sweep*: a simulation based on a saw-tooth speed profile varying between two values.

Analysis label	Duration [s]	Sweep direction
SWP - Long Down	30	Down
SWP - Long Up	30	Up
SWP - Short Down	6	Down
SWP - Short Up	8	Up

Table 3.1: Setup and labels of the *SWP - Monotonic Speed-Sweep* analyses.

3.2.1 Comparison across simulations

In this subsection, the effect of the speed-sweep direction is examined by comparing different analyses. The discussion focuses on the group of simulations referred to as *SWP - Monotonic Speed-Sweep*. The setup and labels of the analyses considered are shown in Table 3.1.

The analysis settings were selected so that the effect of the speed-sweep direction could be evaluated for both long- and short-duration simulations.

Figure 3.6 compares the *SWP - Long Down* and *SWP - Long Up* analyses.

As can be observed, the two Campbell diagrams differ from each other. In particular, the *SWP - Long Down* analysis exhibits more pronounced vertical banding, including in regions that are not affected by this phenomenon in the *SWP - Long Up* analysis. The raw-signal comparison also highlights this difference, with the two simulations exhibiting peaks at different locations and with different amplitudes.

A similar comparison for the short-duration cases is shown in Figure 3.7, which compares the *SWP - Short Down* and *SWP - Short Up* analyses.

Also in this case, the two Campbell diagrams differ from each other. As in the long-duration simulations, the *SWP - Short Down* analysis exhibits more pronounced vertical banding, whereas this phenomenon is not observed in the *SWP - Short Up* analysis.

To assess whether jump phenomena are present, Figure 3.8 shows the first four harmonics associated with both GMF_1 and GMF_2.

As can be seen, no sufficiently sharp amplitude discontinuities or clearly identifiable branch switching can be observed to support the presence of jump phenomena. Therefore, based on the available evidence, the observed differences are more appropriately interpreted in terms of sweep-direction sensitivity, whereas the presence of actual jump phenomena remains unconfirmed.

3.2.2 Within a single simulation

In this subsection, the effect of changes in the speed-sweep direction within the same simulation is examined. The underlying idea of this approach is to analyze the system over a speed range around a known crossing, in order to investigate whether vertical banding may be influenced by changes in the sweep direction, by the progressive increase in simulation time, possibly associated with the accumulation of integration errors, or by a combination of these effects.

For this purpose, a single simulation is performed with the speed varying between two selected values according to a saw-tooth-like profile, as shown in Figure 3.9.

The figure shows the input-shaft speed profile, together with the expected crossing-speed range and the expected crossing times. For comparison purposes,

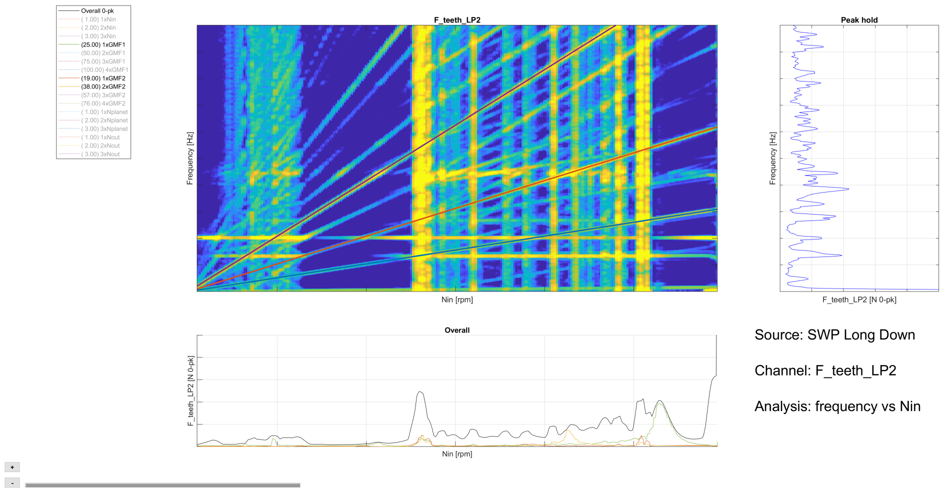

(a) Extended Campbell diagram: *SWP - Long Down*

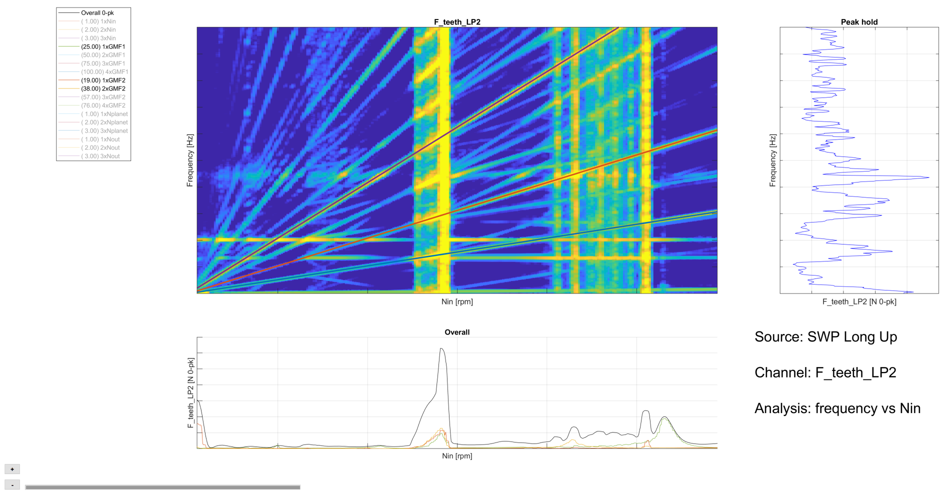

(b) Extended Campbell diagram: *SWP - Long Up*

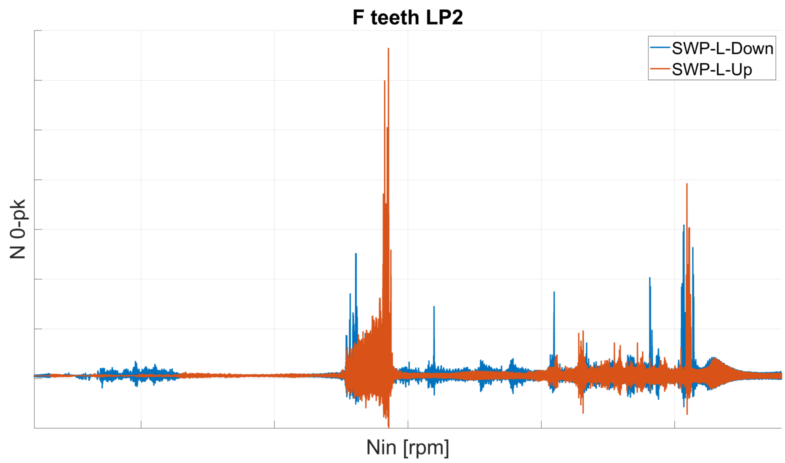

(c) Raw-signal comparison

Figure 3.6: Comparison of the *SWP - Long Down* and *SWP - Long Up* analyses in terms of extended Campbell diagrams and raw signals of the total tooth-contact force of the large planet 2 gear.

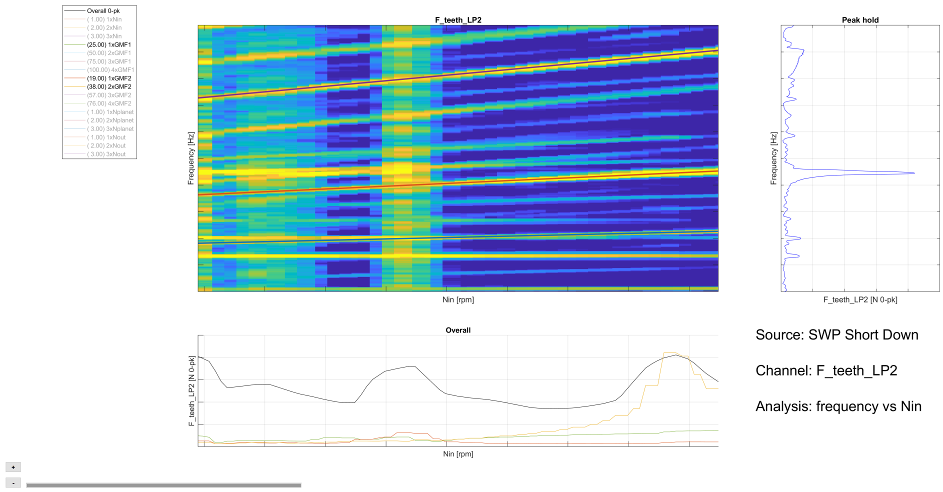

(a) Extended Campbell diagram: *SWP - Short Down*

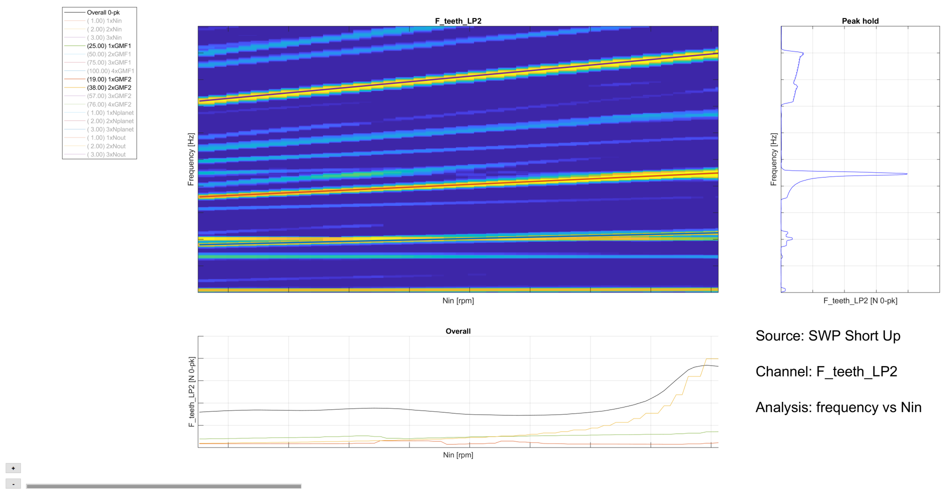

(b) Extended Campbell diagram: *SWP - Short Up*

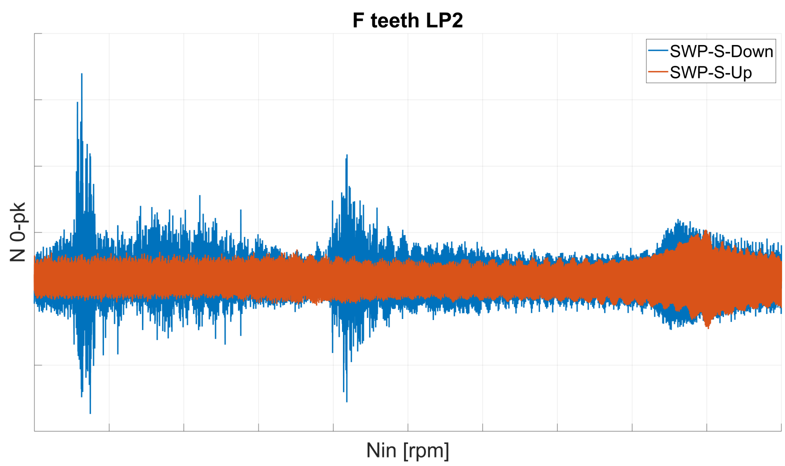

(c) Raw-signal comparison

Figure 3.7: Comparison of the *SWP - Short Down* and *SWP - Short Up* analyses in terms of extended Campbell diagrams and raw signals of the total tooth-contact force of the large planet 2 gear.

GMF_1 harmonics

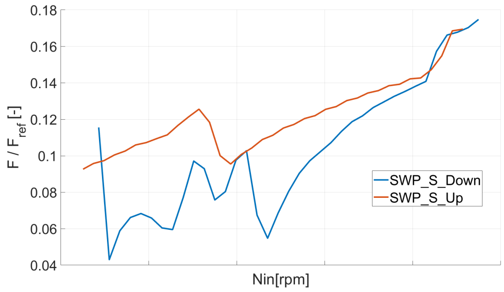

(a) $1 \times GMF_1$

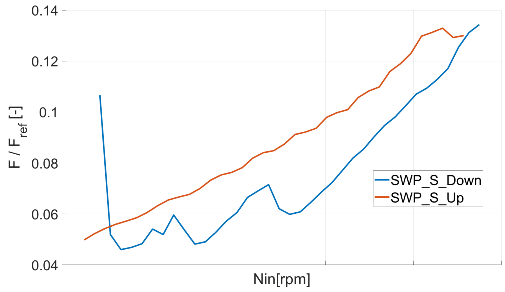

(b) $2 \times GMF_1$

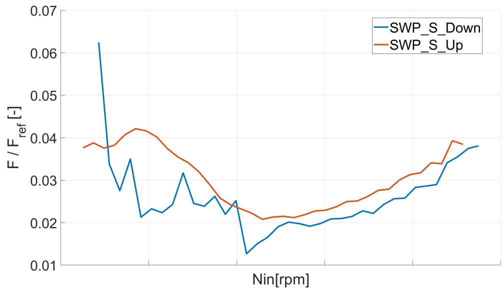

(c) $3 \times GMF_1$

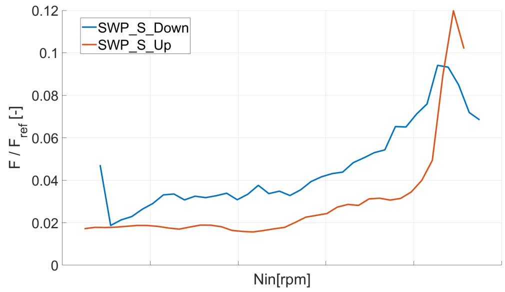

(d) $4 \times GMF_1$

GMF_2 harmonics

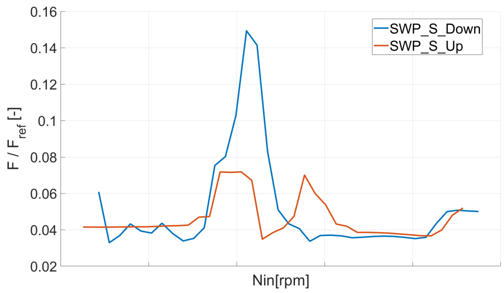

(e) $1 \times GMF_2$

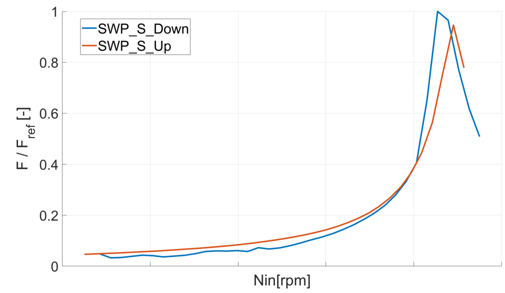

(f) $2 \times GMF_2$

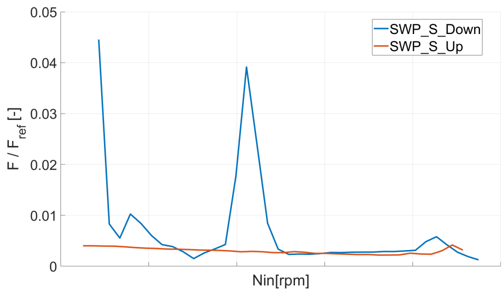

(g) $3 \times GMF_2$

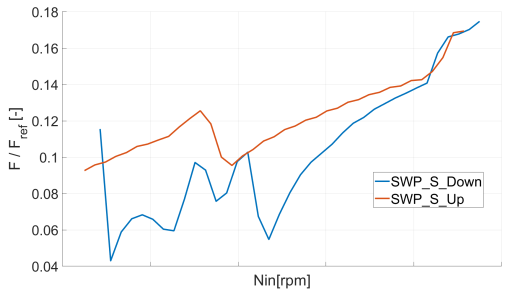

(h) $4 \times GMF_2$

Figure 3.8: Comparison of the first four harmonics of GMF_1 and GMF_2 for the *SWP - Short Down* and *SWP - Short Up* analyses.

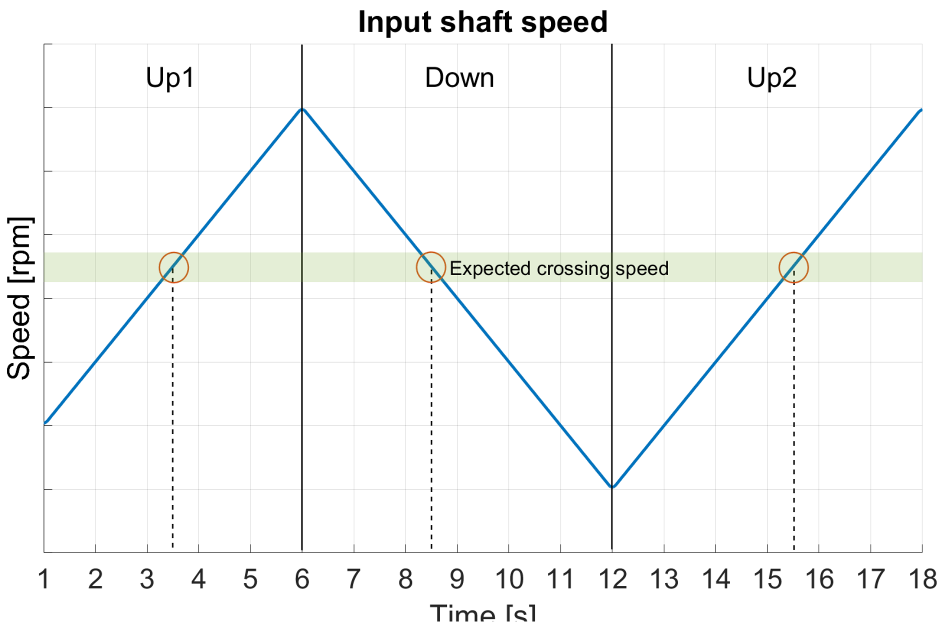

Figure 3.9: Speed profile adopted for the *CYC - Cyclic Speed-Sweep* analysis.

the overall sweep is divided into three parts, each containing a crossing between the $2 \times GMF_2$ excitation line and a system mode within the frequency range of interest:

1. *CYC - Up1*: first part of the overall sweep, in which the speed increases monotonically from the initial value to the maximum value;
2. *CYC - Down*: second part of the overall sweep, in which the speed decreases monotonically from the maximum value to the minimum value;
3. *CYC - Up2*: third part of the overall sweep, in which the speed increases monotonically from the minimum value to the maximum value.

Figure 3.10 shows the comparison for the *CYC - Cyclic Speed-Sweep* analysis. The first three subfigures report the extended Campbell diagrams, together with the corresponding peak-hold spectra and overall responses, for the three portions into which the simulation is divided, namely *CYC - Up1*, *CYC - Down*, and *CYC - Up2*. The raw-signal comparison for the same three portions is shown in Figure 3.10d.

As can be observed in the first three subfigures of Figure 3.10, no vertical banding is present, and the three portions of the simulation are broadly consistent with one another. Minor discrepancies can be observed in the Campbell diagram corresponding to *CYC - Up2*. However, the peak-hold spectrum does not reveal any significant differences with respect to the other portions. This suggests that the observed deviations are not substantial and are limited to negligible components, possibly associated with the accumulation of integration error over the simulation time.

The main differences identified concern the peak amplitudes and the speed at which the corresponding peaks occur. In particular, the peak measured in *CYC - Down* is higher than the corresponding peak in the other portions of the simulation. Moreover, the crossing speed appears to be lower in this portion than in the other two, as can also be seen in the raw-signal comparison shown in Figure 3.10d.

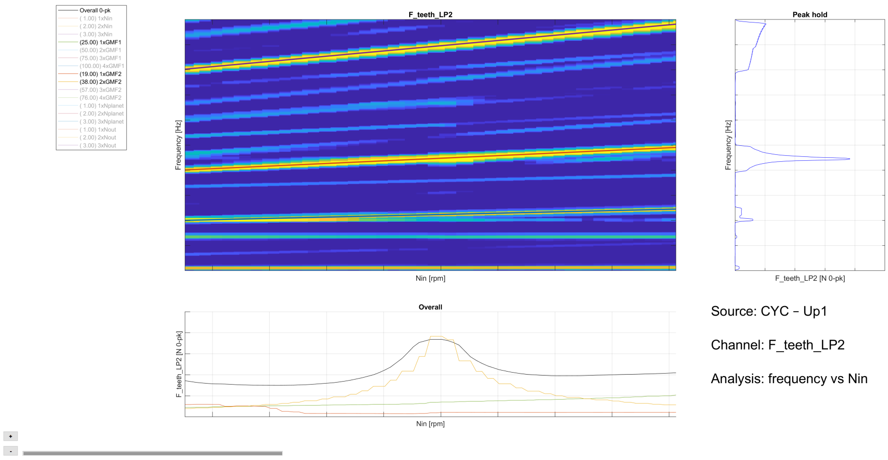

(a) Extended Campbell diagram: *CYC - Up1*

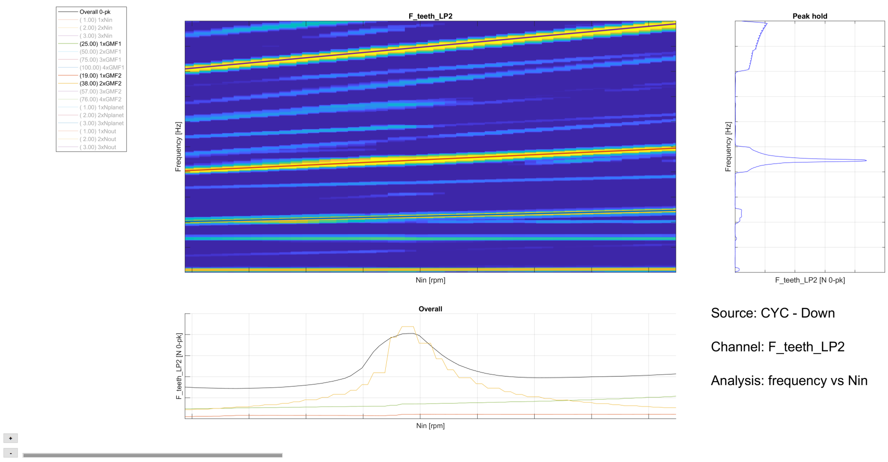

(b) Extended Campbell diagram: *CYC - Down*

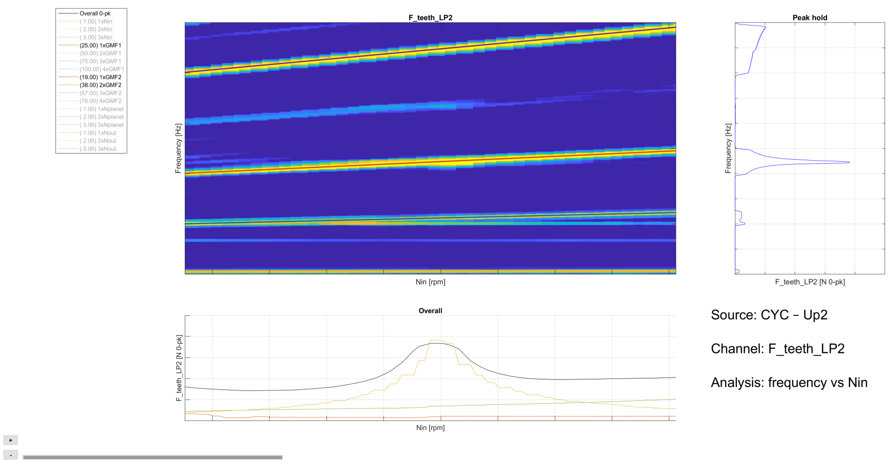

(c) Extended Campbell diagram: *CYC - Up2*

Figure 3.10: Comparison of the extended Campbell diagrams, including peak-hold spectrum and overall response, for the three portions of the *CYC - Cyclic Speed-Sweep* analysis, together with the corresponding raw-signal comparison.

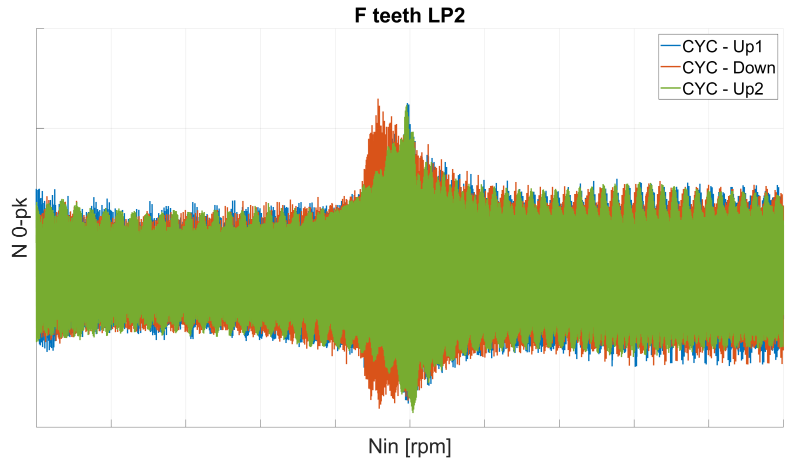

(d) Raw-signal comparison

Figure 3.10: Comparison of the Campbell diagrams and raw signals for the *CYC - Cyclic Speed-Sweep* analysis (continued).

3.2.3 Overall comparison

This subsection provides an overall comparison of all the cases discussed in this section.

Figure 3.11 shows the comparison of the second harmonic of GMF_2 for all the analyses considered. This is the dominant excitation source within this speed range. The plot indicates that the *CYC* simulation and the short-duration *SWP* analyses produce nearly overlapping results when the sweep direction is the same. By contrast, the long-duration *SWP* analyses differ significantly from both the short-duration *SWP* cases and the *CYC* simulation; however, this difference is consistent with the effects discussed in subsection 3.1.3. The effect of the sweep direction is more clearly reflected in the peak location and amplitude, with downward sweeps exhibiting a peak at a lower speed and with a higher amplitude than the corresponding upward sweeps.

A possible interpretation of this behavior emerged from the subsequent modal analysis discussed in section 5.2. The peak associated with the $2 \times GMF_2$ crossing is located approximately midway between the natural frequencies of the two complex-conjugate system modes, Modes 4.1 and 4.2. These two modes exhibit essentially the same modal shape, differing only in the direction of propagation of the associated traveling wave. Under ideal conditions, they would be expected to have the same, or nearly the same, natural frequency. In the present case, however, a non-negligible separation was observed between their natural frequencies. This may be related to the fact that the eigenvalue analysis is performed by linearizing the system about a nonlinear operating condition involving contact, possibly combined with numerical inaccuracies. Within this interpretation, the sweep direction may affect the response because the crossing region is approached from opposite sides, so that one or the other of the two nearby modes may be encountered first. Although this hypothesis was not verified conclusively, it is consistent with the observed differences in peak location and amplitude between upward and downward sweeps.

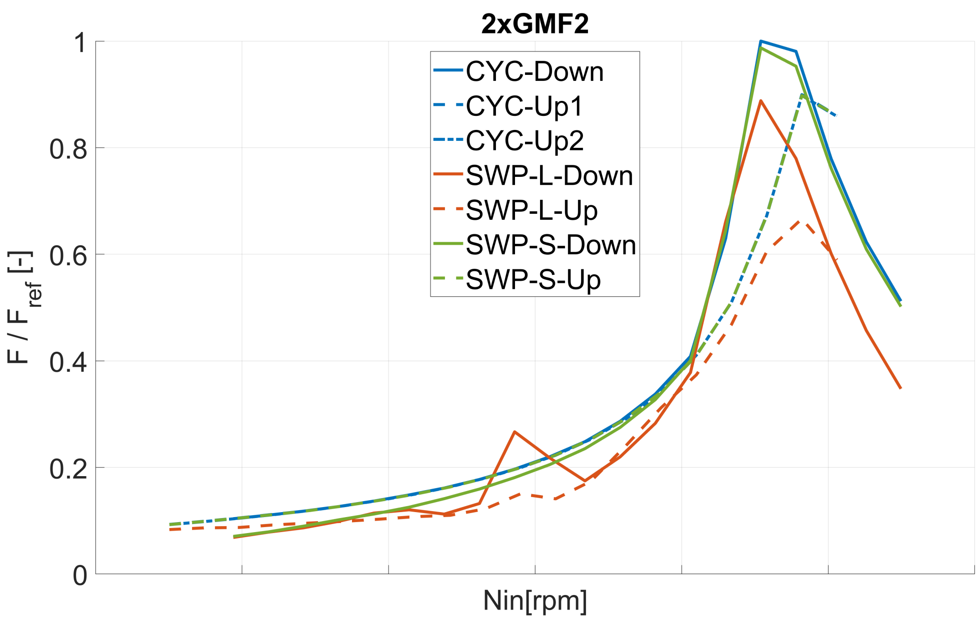

Figure 3.11: Comparison of the $2 \times GMF_2$ excitation component for all the *SWP - Monotonic Speed-Sweep* and *CYC - Cyclic Speed-Sweep* analyses.

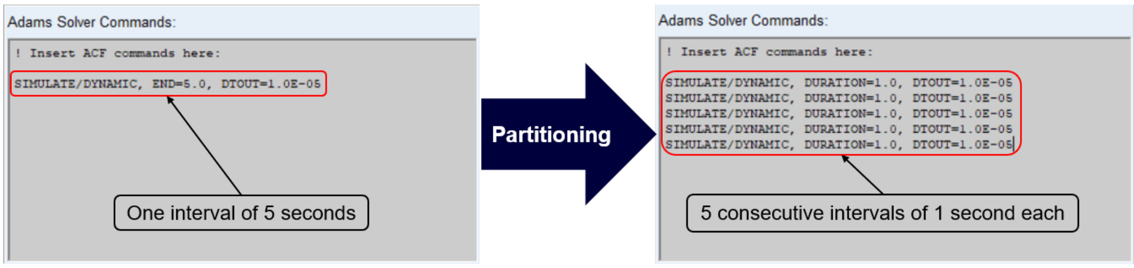

Figure 3.12: Example of time-interval partitioning in an *MSC Adams* simulation.

3.3 Effects of time-interval partitioning

This section examines the effect of time-interval partitioning, beginning with a brief introduction to the reasons for splitting the overall simulation interval into consecutive sections.

In *MSC Adams*, especially in long-duration simulations, it is good practice to divide the overall simulation time into consecutive sub-intervals. At the end of each sub-interval, the system state is saved and used as the initial condition for the next one. This procedure is intended to prevent the accumulation of numerical error by restarting the simulation at regular intervals.

Figure 3.12 shows how time-interval partitioning is implemented. Instead of defining a single *Adams Solver* command for a dynamic analysis over a given duration, the same command is repeated multiple times over shorter time intervals. The software executes the commands sequentially and, when passing from one command to the next, the accumulated numerical integration error is effectively reset at each restart.

This practice offers an additional advantage. During a simulation performed with the *MSC Adams - External Solver*, the software provides simulation feedback

Analysis label	Duration [s]	Sweep direction	Partitioning
Up-P1	6	Up	No partitioning
Up-P2(5+2)s	7	Up	5 s + 2 s
Down-P2(5+3)s	8	Down	5 s + 3 s
Down-P4(2s)	8	Down	4 × 2 s
Down-P16(0.5s)	8	Down	16 × 0.5 s

Table 3.2: Setup of the analyses used to assess the effect of time-interval partitioning on the simulation results.

only at every 10% of completion of the running command. For long simulations, this would imply extended periods without feedback. The time-interval-partitioning approach makes it possible to split a single command into multiple shorter ones, thereby providing more frequent feedback and improving monitoring of the simulation progress. It should be noted that, for the cases analyzed in this thesis, no significant increase in the total computation time was observed with respect to cases in which time-interval partitioning was not used.

The next subsections present the analysis settings and discuss the effect of time-interval partitioning on the results. The section concludes with the selection of a sub-interval size to be adopted in the subsequent simulations discussed in this thesis.

3.3.1 Simulation setup

To assess the effect of time-interval partitioning on the results, the simulations listed in Table 3.2 are performed.[1]

The analysis setup was defined so as to assess the effect of the sub-interval size for both upward and downward speed-sweep analyses.

3.3.2 Comparison and choice of partitioning

This subsection discusses the effect of time-interval partitioning and the influence of the chosen sub-interval size.

Figure 3.13 shows the first four harmonics associated with both GMF_1 and GMF_2 for all the analyses listed in Table 3.2.

As can be observed, no relevant differences associated with the sub-interval size are found in the dominant excitation source, namely $2 \times GMF_2$. However, some differences can be identified in other non-negligible harmonics. In particular, partitioning appears to have a negligible effect on upward speed-sweep analyses. By contrast, it has a stronger influence on the results of downward speed-sweep analyses, especially with respect to the chosen sub-interval size.

Figure 3.14 shows the extended Campbell diagrams, including peak-hold spectrum and overall response, for the *Down-P2(5+3)s*, *Down-P4(2s)*, and *Down-P16(0.5s)* analyses, ordered from coarser to finer time-interval partitioning. It

[1] The naming convention adopted for the analyses follows the scheme: speed-sweep direction - number of sub-intervals into which the analysis duration is divided - information on the sub-interval size. For example, the simulation named *Up-P2(5+2)s* is an upward speed-sweep divided into two sub-intervals of 5 and 2 seconds, respectively.

GMF_1 *harmonics*

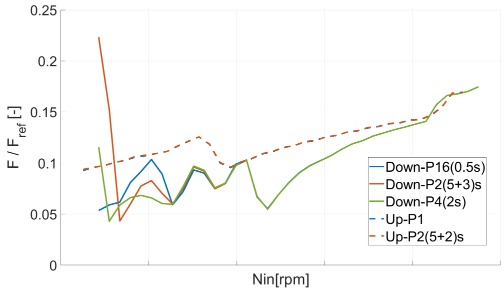

(a) $1 \times GMF_1$

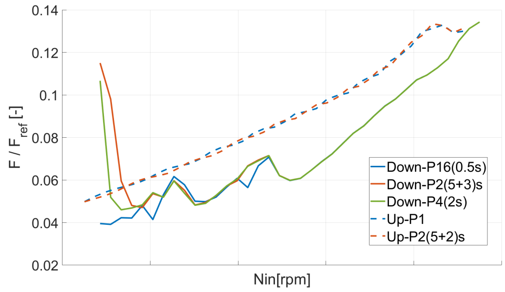

(b) $2 \times GMF_1$

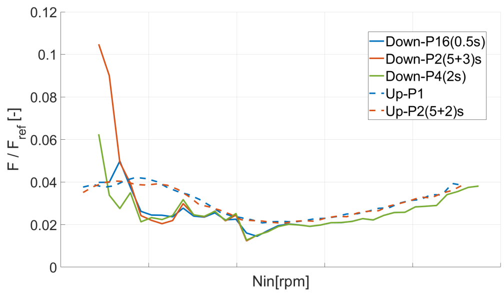

(c) $3 \times GMF_1$

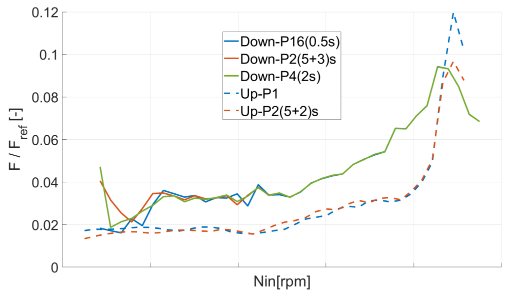

(d) $4 \times GMF_1$

GMF_2 *harmonics*

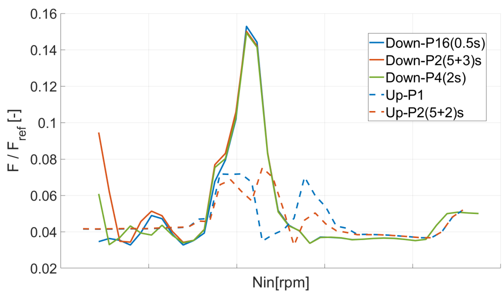

(e) $1 \times GMF_2$

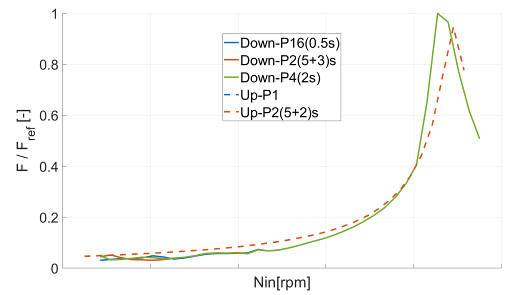

(f) $2 \times GMF_2$

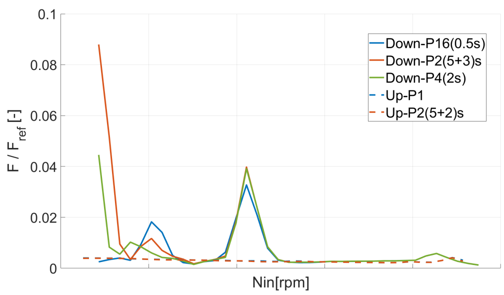

(g) $3 \times GMF_2$

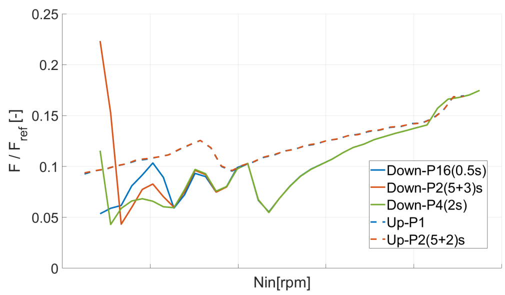

(h) $4 \times GMF_2$

Figure 3.13: Comparison of the first four harmonics of GMF_1 and GMF_2 for the partitioning-sensitivity analyses.

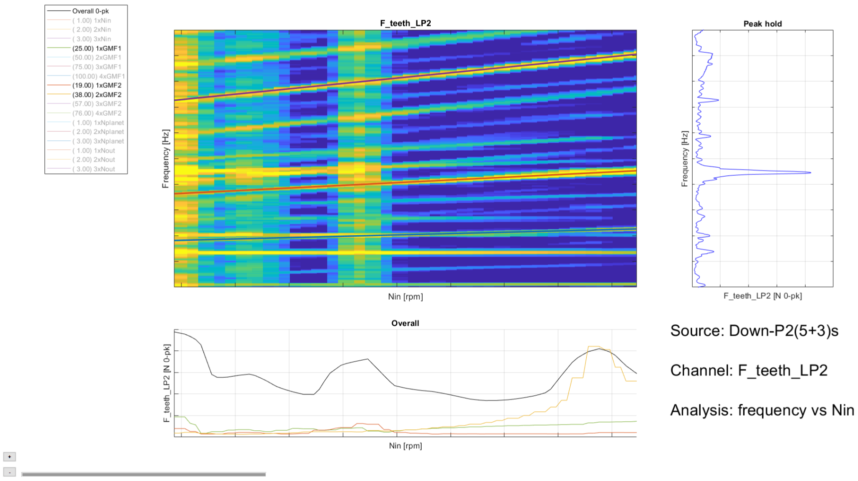

(a) Extended Campbell diagram: *Down-P2(5+3)s*

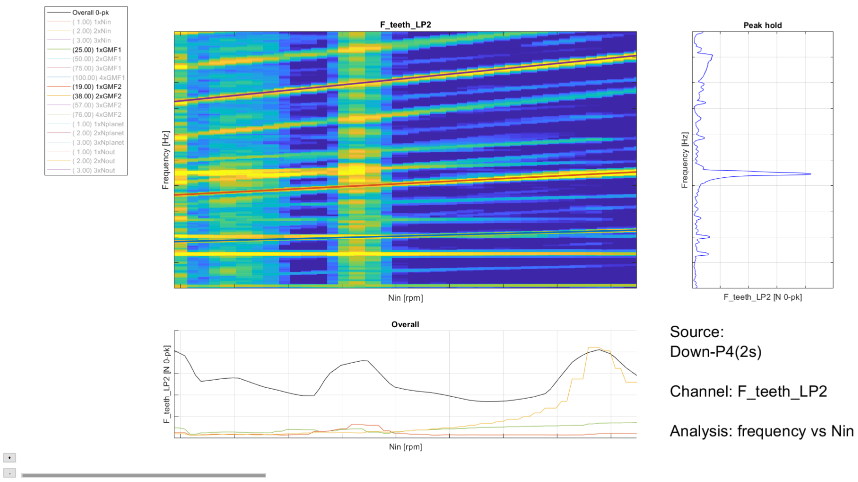

(b) Extended Campbell diagram: *Down-P4(2s)*

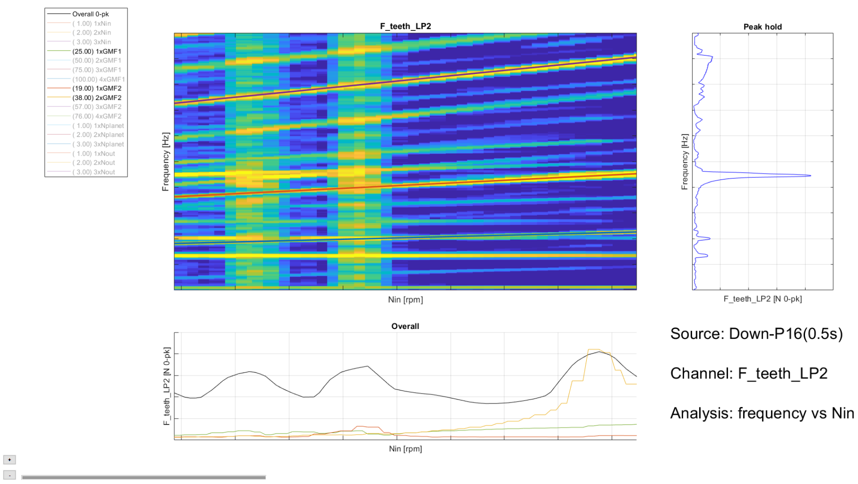

(c) Extended Campbell diagram: *Down-P16(0.5s)*

Figure 3.14: Extended Campbell diagrams, including peak-hold spectrum and overall response, for the *Down-P2(5+3)s*, *Down-P4(2s)*, and *Down-P16(0.5s)* analyses.

can be observed that reducing the sub-interval size mitigates the vertical-banding phenomenon. In particular, when moving from a mean sub-interval size of 4 seconds to 2 seconds and finally to 0.5 seconds, one of the vertical bands gradually disappears.

For this reason, a sub-interval size of 0.5 seconds is adopted for the subsequent analyses presented in this thesis.

Taken together, the analyses discussed in this chapter show that analysis duration, sweep direction, and sub-interval size all influence the simulation results and, in particular, the occurrence and intensity of vertical banding. While these parameters affect the response in different ways, their influence must be taken into account in order to define a reliable simulation setup for the subsequent analyses. The main trends identified throughout the chapter are summarized in Table 3.3.

Parameter	Condition	Observed trend
Analysis duration	Longer	More pronounced vertical banding
Analysis duration	Shorter	Reduced banding; greater consistency
Sweep direction	Downward	More pronounced vertical banding
Sweep direction	Upward	Less pronounced vertical banding
Sub-interval size	Coarser	More evident vertical banding
Sub-interval size	Finer	Reduced vertical banding

Table 3.3: Summary of the observed effects of analysis duration, sweep direction, and sub-interval size on the simulation results.

Chapter 4

Assessment of Numerical Results

In this chapter, the numerical results obtained with *MSC Adams* are assessed by comparing selected simulated quantities with their corresponding theoretical values. This comparison was also initially motivated by the need to investigate the origin of the vertical banding observed in the Campbell diagrams. In particular, one possible explanation considered at the outset was the presence of a progressive angular-position error in the gear components, potentially leading to local tooth interference and impulsive contact events during the simulation. The analyses presented in this chapter do not support that hypothesis; rather, they suggest that no cumulative angular-position error is observed within the examined conditions.

The quantities selected for the numerical-to-theoretical comparison are the angular position, angular velocity, angular acceleration, and transmitted torque of selected gears. For confidentiality reasons, all the reported plots are normalized between 0 and 1 using the corresponding theoretical reference. Moreover, whenever a difference between numerical and theoretical values is reported, it is computed between the normalized values of the two quantities.

The chapter begins with an introduction to the *MSC Adams Orient gears* command, together with the setup of the baseline analysis. The subsequent section presents the results of the comparison and includes a discussion of the remaining discrepancy between the numerical and theoretical datasets, together with some considerations on the dynamic symmetry of the model.

4.1 Preliminary Tools and Analysis Setup

The present section introduces the *Orient gears* command, which allows the gears to be oriented automatically by the software. It then presents the setup of the baseline simulation used for the validation of the numerical results.

4.1.1 *Orient gears* Command

In *MSC Adams*, the *Gear AT* tool is used to define and manage gear components. In particular, each gear is described through two main tabs: *Gear AT Element* and *Gear AT Force*. The former contains the geometric specifications of the gear, together with references to the files used to generate the component. The latter contains the parameters used to define the interaction forces and torques between the gear and the mating components, including contact and friction effects.

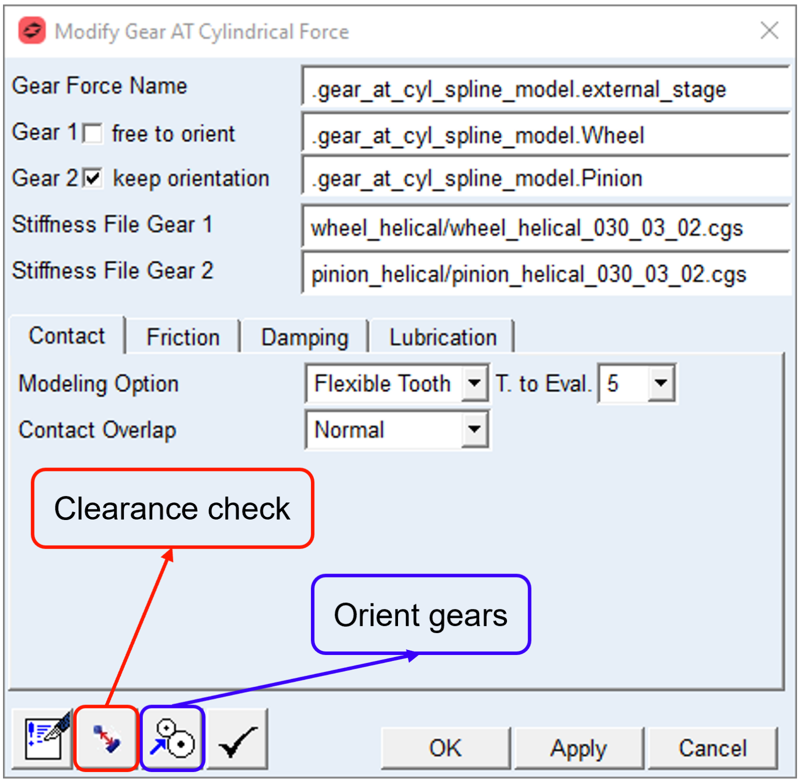

Figure 4.1: *Gear AT Force* creation window, with the *Clearance check* and *Orient gears* commands highlighted.

Once the gear elements have been created, a *Gear AT Force* must be defined for each pair of meshing gears. The *Gear AT Force* creation window is shown in Figure 4.1.

After the *Gear AT Force* has been created, it is possible to evaluate the minimum distance between the teeth of the two gears, which the software defines as *clearance*. This value can be positive, meaning that there is still space between the teeth of the two gears and that they are not yet in contact, or zero, meaning that the gears are in contact. If tooth interpenetration occurs, the software reports the condition as *Penetration*. This quantity can be evaluated by means of the *Clearance check* command.

If the user wants to modify the *clearance* value, the *Orient gears* command can be used. First, the user must specify which gear is allowed to rotate during the procedure. This can be done by selecting or clearing the box next to "Gear 1" and "Gear 2." If a gear is labeled as "free to orient," the software rotates it to minimize the *clearance* and avoid interpenetration. Conversely, if a gear is labeled as "keep orientation," its angular position is left unchanged. Therefore, in order to execute the *Orient gears* command, at least one of the two gears must be set to "free to orient".

Unfortunately, the *Orient gears* command does not guarantee equal *clearance* between the sun gear and all the planet gears of a planetary stage. As a result, an iterative procedure based on the two commands described above, together with manual reorientation, is required.

Most of the information reported in this section can be found in the *Gear AT* > *Gear AT Force* > *New Gear AT Force* > *Main* section of the Adams Machinery

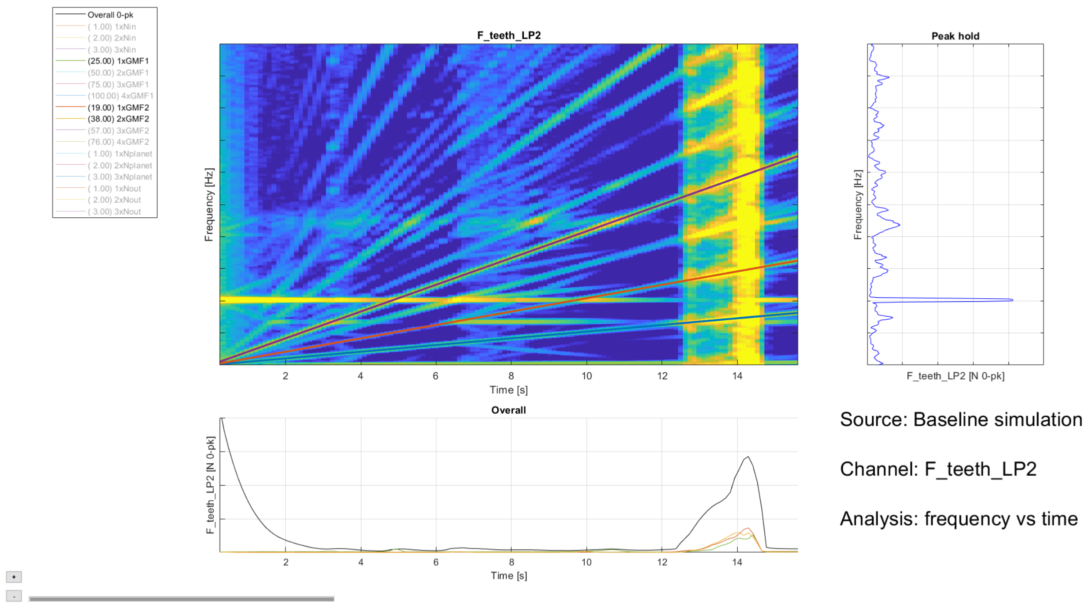

Figure 4.2: Extended Campbell diagram for the baseline simulation, including the peak-hold spectrum and overall response.

User's Guide [2].

In the present work, this command was later used to modify the relative orientation of meshing gears in order to investigate the angular-position discrepancies discussed later in this chapter.

4.1.2 Analysis Setup

The analysis considered for this comparison is an increasing speed-sweep with constant angular acceleration, starting from standstill. Its total duration is 16 s, divided into 32 sub-intervals of 0.5 s each. The model also includes a resistant torque applied to the ring gear, representing the contribution of the propeller and output-shaft inertia. In order to avoid unnecessarily complicating the theoretical description of the system, this torque was assumed to be equal to its steady-state value from the beginning of the analysis. The derivation of the reference quantities is reported in Appendix A.

Figure 4.2 shows the extended Campbell diagram of the baseline simulation, in which the vertical banding phenomenon that motivated the present investigation is still visible.

The time interval over which this phenomenon occurs will be highlighted by a gray-shaded region in the plots presented later in this chapter.

4.2 Results and Discussion

This section presents the validation of the numerical results through a numerical-to-theoretical comparison of the main kinematic and dynamic quantities.

For each gear, the monitored quantities are angular position, angular velocity, angular acceleration, and transmitted torque.

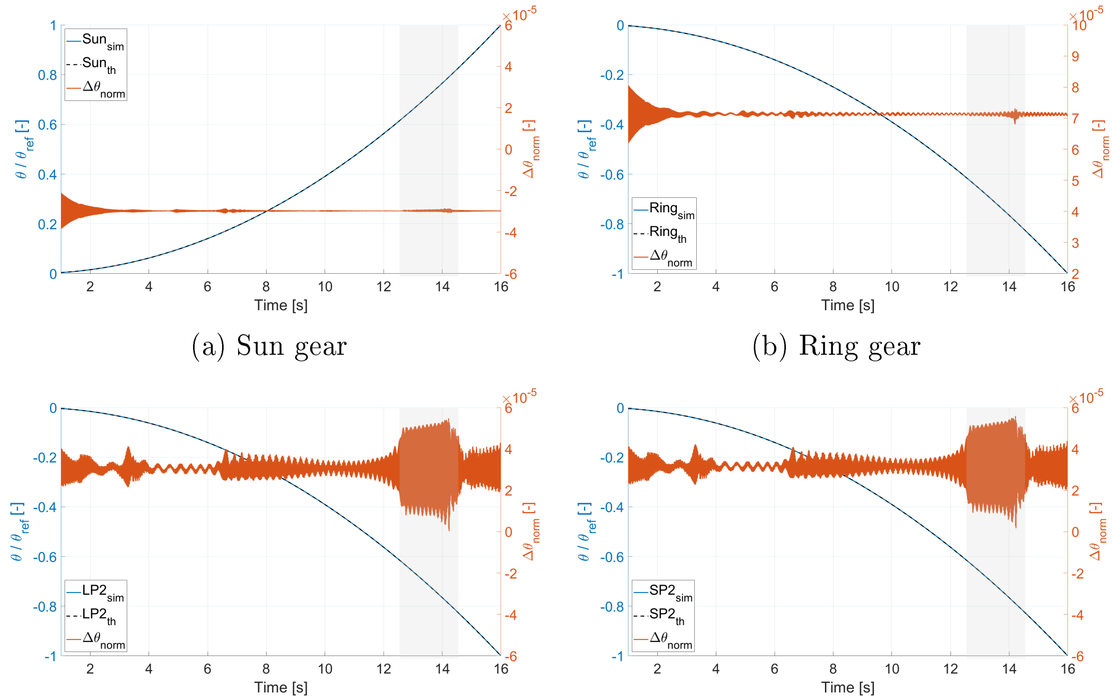

(a) Sun gear

(b) Ring gear

(c) Large planet gear 2

(d) Small planet gear 2

Figure 4.3: Comparison of normalized numerical and theoretical angular positions, together with the corresponding normalized difference, for the sun gear, ring gear, large planet gear 2, and small planet gear 2 in the baseline simulation.

4.2.1 Angular Positions

This subsection presents the comparison between the numerical and theoretical angular positions of selected gears in the reduction gearbox.

Figure 4.3 shows, for the sun gear, ring gear, large planet gear 2, and small planet gear 2, the comparison between the normalized numerical and theoretical angular-position time histories on the left vertical axis, together with the corresponding normalized difference on the right vertical axis. In particular, both the numerical and theoretical angular positions are normalized between 0 and 1 using the minimum and maximum values of the theoretical dataset. The reported difference is therefore defined as

$$\Delta\theta_{\text{norm}} = \theta_{\text{num,norm}} - \theta_{\text{th,norm}}$$

The plots for the other planet gears are not reported because they exhibit trends similar to those shown here. This is consistent with the calibrated orientation of the planet gears obtained through the *Orient gears* command, following the procedure described in subsection 4.1.1.

Table 4.1 summarizes the effect of the reorientation procedure. Focusing on the first reduction stage, the large planet gears initially exhibited different clearances with respect to the sun gear, as shown in the "Before reorientation" column. This difference may have led to different meshing instants between the planet gears and the sun gear, which is consistent with the different mean values of $\Delta\theta_{norm}$ observed before reorientation. By equalizing the clearance values through the procedure described above, the values reported in the "After reorientation" column were obtained.

Large planet gear	Before reorientation	After reorientation
Planet gear 1	0.145	0.032
Planet gear 2	Penetration	0.032
Planet gear 3	Penetration	0.032

Table 4.1: Clearance values between the sun gear and the large planet gears of the first reduction stage before and after reorientation.

Correspondingly, the mean values of $\Delta\theta_{norm}$ for the planet gears appear to align.

As can be observed from Figure 4.3, the numerical datasets follow the corresponding theoretical ones closely. Their difference oscillates around an approximately constant value throughout the simulation, suggesting that no significant cumulative trend is present. The main remaining discrepancy is that this difference oscillates around nonzero values. The possible origin of this feature will be discussed in subsection 4.2.2.

A further observation can also be made. The $\Delta\theta_{norm}$ differences between the large and small planet gears mounted on the same layshaft are negligible. This suggests that the observed oscillations of these gears are largely rigid-body in nature and are therefore likely associated with the motion of the layshaft as a whole. These oscillations could potentially be reduced by properly tuning the damping parameters in the contact definition of the *Gear AT Force* in *MSC Adams*.

4.2.2 Interpretation of the Angular-Position Offset

In the plots shown in Figure 4.3, the difference between the normalized numerical and theoretical datasets oscillates around a constant nonzero value. In particular, considering the sign convention adopted for the angular position of each gear, which is positive for the sun gear and negative for the other gears, together with the definition of $\Delta\theta_{norm}$, a consistent trend can be observed. The sun gear exhibits a negative mean value of $\Delta\theta_{norm}$, whereas the other gears oscillate around positive values. This suggests that the theoretical values tend to remain greater in absolute value than the corresponding numerical ones over most of the simulation.

A possible explanation for this offset is the flexibility of the bodies in the model, which is not accounted for in the theoretical derivation of the reference quantities. In particular, for the sun gear, the imposed motion is applied at the marker located at the beginning of the input shaft. The flexibility of the shaft may therefore introduce a delay in the onset of the sun-gear rotation.

To assess this hypothesis, a new simulation was performed. All parameters were kept unchanged with respect to the baseline simulation, except for the point of application of the imposed motion. In this case, the motion was applied directly to the marker associated with the sun gear, which is also the reference marker used to define the corresponding *Gear AT Element* and is located at the geometric center of the sun gear.

Figure 4.4 shows, for the sun gear and ring gear, and similarly to the baseline simulation, the comparison between the normalized numerical and theoretical angular-position time histories on the left vertical axis, together with the corresponding normalized difference on the right vertical axis.

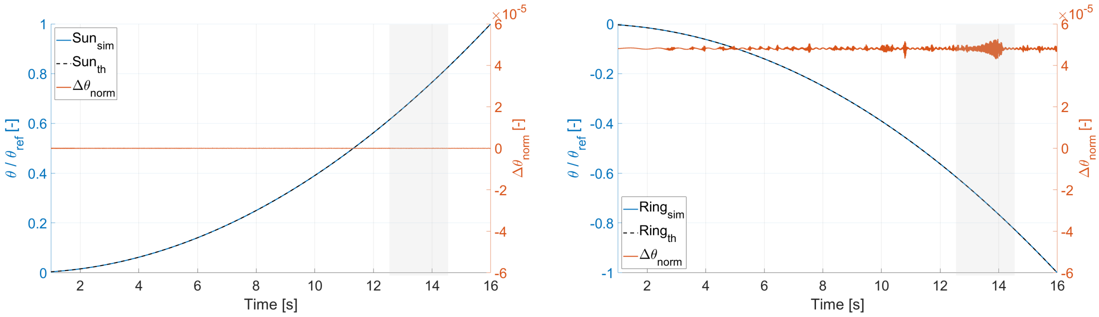

(a) Sun gear (b) Ring gear

Figure 4.4: Comparison of normalized numerical and theoretical angular positions, together with the corresponding normalized difference, for the sun gear and ring gear in the sun-motion simulation.

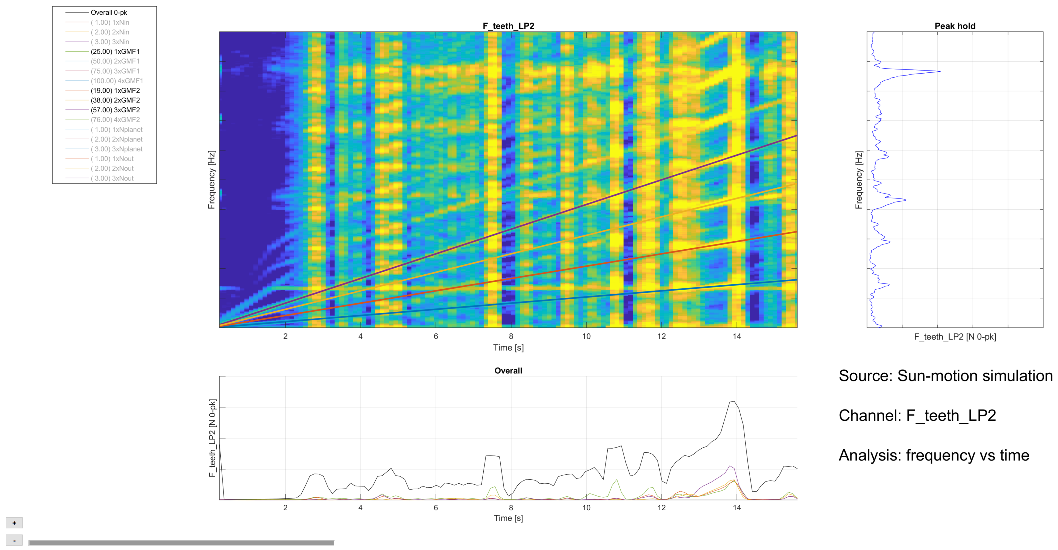

Figure 4.5: Extended Campbell diagram for the sun-motion simulation, including the peak-hold spectrum and overall response.

Looking at the sun-gear plot, it can be observed that the offset previously affecting the mean value of $\Delta\theta_{norm}$ is no longer visible. This result supports the interpretation that, for the sun gear, the previously observed delay was associated with the flexibility of the input shaft. For the ring gear, by contrast, the offset is still present. This residual offset may be related to the clearance and backlash effects associated with meshing gears in the gearbox. Since the theoretical discussion assumes that all gears start rotating instantaneously, these effects may introduce a delay in the numerical response with respect to the theoretical one.

For completeness, the extended Campbell diagram of the sun-motion simulation, together with the peak-hold spectrum and overall response, is shown in Figure 4.5.

As can be observed, the Campbell diagram exhibits a much more pronounced vertical banding phenomenon than that observed in the baseline simulation shown in Figure 4.2. This is consistent with the higher level of noise and the more spiky character of the numerical signals obtained in the sun-motion simulation. Since the physical conditions of the system remain unchanged, such as rotational speeds and applied torques, and only the boundary conditions of the model are modified, this result suggests that the vertical banding is a numerical artifact. Its exact origin, however, remains unclear.

Although this configuration resolves the offset observed at the sun gear, it was not adopted as the reference one. In fact, the higher noise level and the more pronounced vertical banding lead to a larger number of spurious peaks and to an overall deterioration in signal quality. For this reason, in the remainder of the work, the imposed motion was kept at its original application point, upstream of the input shaft.

4.2.3 Angular Velocities and Accelerations: HHT-I3 Solver Limitations

This subsection presents the comparison between the numerical and theoretical angular velocities and angular accelerations of selected gears in the reduction gearbox.

The upper part of Figure 4.6 shows the angular velocities of the sun gear, ring gear, and large planet gear 2. The plots for the other gears are not reported because they exhibit trends similar to that of large planet gear 2. For each gear, the angular-velocity plots compare the numerical and theoretical angular-velocity time histories on the left vertical axis. Each quantity is normalized between 0 and 1 using the minimum and maximum values of the theoretical dataset. Similarly to the angular-position plots, the right vertical axis shows the difference between the two normalized quantities:

$$\Delta\omega_{\text{norm}} = \omega_{\text{num,norm}} - \omega_{\text{th,norm}}$$

The lower part of Figure 4.6 shows the angular accelerations of the sun gear, ring gear, large planet gear 2, and small planet gear 2. The plots for the other gears have been omitted because they are similar to those of large and small planet gear 2. By contrast, the angular-acceleration plots show only the numerical and theoretical signals, together with a moving-average curve obtained from the numerical data using the *movmean* function in *MATLAB* [8]. Since the theoretical angular acceleration is constant, the normalization is performed with respect to its theoretical value. Because of the high noise level in the numerical signal, the moving average is used to track its mean evolution throughout the simulation. Its purpose is to assess whether this trend remains approximately constant or varies during the analysis.

As can be observed from the plots, no significant cumulative trends can be identified during the simulation in either $\Delta\omega_{norm}$ or the moving average of the angular acceleration. Similarly to the case of angular positions, this suggests that the numerical results remain overall consistent with the corresponding theoretical trends. At the same time, the numerical signal becomes progressively noisier and more spiky when moving from angular positions to angular velocities and, finally, to angular accelerations. This behavior can be attributed to the solver adopted for the present analysis, namely the *HHT-I3* solver. As a reduced-order solver, it monitors the integration error only in the system displacements. Consequently, strict consistency of velocities and accelerations with the first and second time derivatives of the displacement field is not enforced, which results in noisy and spiky signals. This behavior is documented in the *About Adams Solver > Conventions > Guidelines for Solver Selection and Settings > HHT* section of the Adams Solver User's Guide [6] and in

Angular velocities

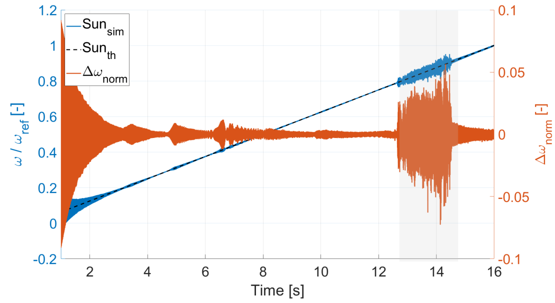

(a) Sun gear

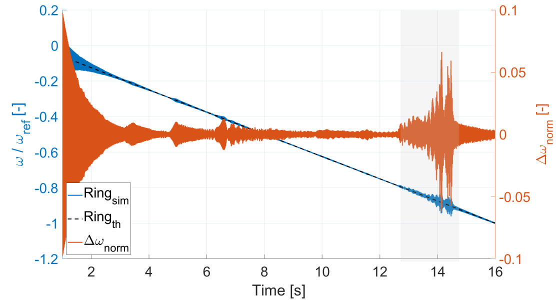

(b) Ring gear

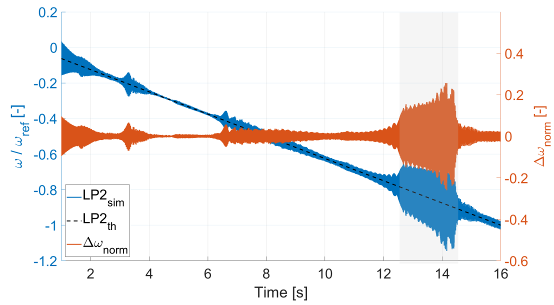

(c) Large planet gear 2

Angular accelerations

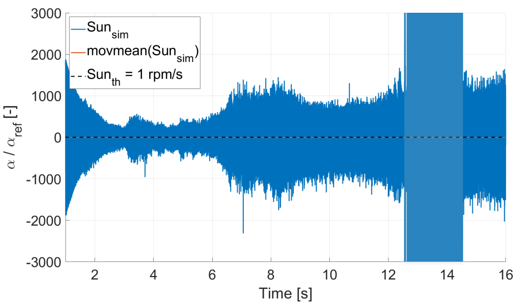

(d) Sun gear

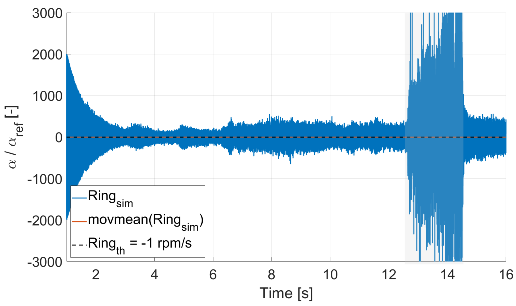

(e) Ring gear

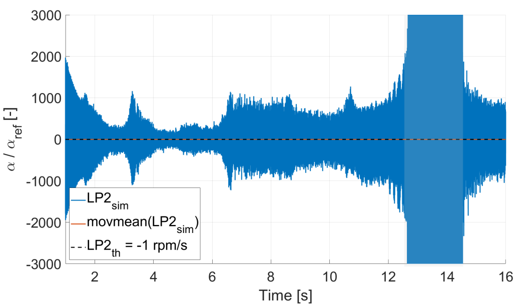

(f) Large planet gear 2

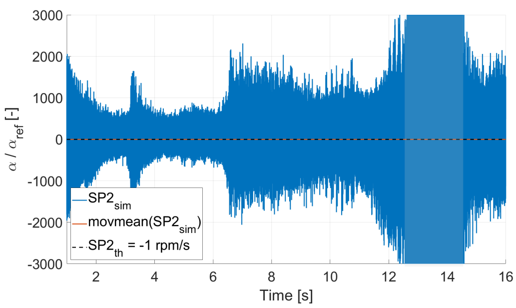

(g) Small planet gear 2

Figure 4.6: Comparison of normalized numerical and theoretical angular velocities and angular accelerations for selected gears in the baseline simulation.

the *Testing Models > Simulation Basics > About Dynamic Simulations > Equation Formulation Comparison > I3* section of the Adams View User's Guide [9].

4.2.4 Transmitted Torque

This subsection presents the transmitted torque for selected gears in the reduction gearbox.

In *MSC Adams*, when a *Gear AT Force* is defined between two gear elements, the *Total Force and Torque* can be exported for each gear along the x, y, and z directions. These quantities represent the time histories of the forces and torques transmitted to or by that gear. The coordinate system adopted by the software, together with the available output requests, is documented in the *Gear AT > Gear AT Results > Requests* section of the Adams Machinery User's Guide [2].

The plots in Figure 4.7 show the time evolution of the total torque along the z direction for the sun gear and the ring gear. In the reference system adopted by *MSC Adams*, the z axis is aligned with the gear rotation axis. The numerical datasets are normalized with respect to the corresponding constant theoretical torque of each gear, and the sign convention is consistent with that adopted for the other quantities. Each plot shows the total torque exchanged by either the sun gear or the ring gear with the meshing planet gears, together with the individual contributions associated with each of them. For this reason, the torque plots for the planet gears are not reported separately, since the relevant qualitative information is already contained in the plots of the sun and ring gears, while the adopted normalization prevents any meaningful quantitative comparison among the exchanged torque levels.

As can be observed from the plots, the numerical datasets are consistent, in terms of mean value, with the corresponding theoretical values. However, differences can still be observed in the oscillatory contribution associated with the individual planet gears and in the torque portions exchanged with them by the sun and ring gears. This suggests that the model is symmetric in its mean, quasi-static response, whereas this symmetry is not fully preserved in the dynamic component of the torque response.

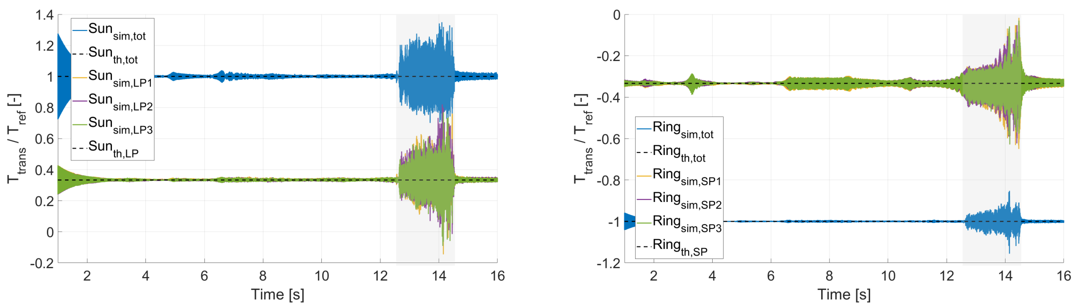

(a) Sun gear (b) Ring gear

Figure 4.7: Comparison of normalized numerical and theoretical transmitted torque for the sun gear and ring gear in the baseline simulation.

4.2.5 Summary of Main Findings

Overall, the analyses presented in this chapter indicate that the numerical results are broadly consistent with the corresponding theoretical trends, since no significant cumulative error trends can be identified during the simulation. In addition, the *Orient gears* command was used to equalize the clearance between the sun gear and each planet gear, thereby restoring the symmetry of the mean angular-position differences among the planets. At the same time, the analyses highlight some limitations of the adopted *HHT-I3* solver, particularly in the velocity and acceleration signals, which are affected by noise and spurious peaks. The results also suggest that the model preserves symmetry in its mean response, whereas the oscillatory component does not exhibit the same degree of symmetry. In addition, the stronger vertical banding observed after modifying only the boundary conditions supports the interpretation of this phenomenon as numerical in nature, although its exact origin remains unresolved. For this reason, the imposed motion was kept applied upstream of the input shaft, since the alternative configuration led to noisier signals and more pronounced vertical banding.

Chapter 5

Modal analysis

This chapter presents the modal analysis feature available in *MSC Adams*. It first outlines the procedure used to perform the modal analysis in this software and then examines the variation of the computed natural frequencies over the simulation time.

In the present work, only the first six mode shapes, ordered by increasing natural frequency, are considered. More specifically, the first two mode shapes are identified as a complex-conjugate pair and are labeled as Modes 1.1 and 1.2. The third and fourth mode shapes are treated as individual modes and are therefore labeled as Modes 2 and 3, respectively. The fifth and sixth mode shapes are identified as a second complex-conjugate pair and are labeled as Modes 4.1 and 4.2.

For confidentiality reasons, all values are reported in normalized form. The normalization is based on reference mean values computed by averaging only the samples within predefined admissible ranges, thereby excluding numerical outliers. In particular, Modes 1.1 and 1.2 are normalized using the reference mean value of Mode 1.2; Modes 2 and 3 are each normalized using their own reference mean value; and Modes 4.1 and 4.2 are normalized using the reference mean value of Mode 4.2.

The chapter concludes with a discussion of the parameters that affect the computed natural frequencies.

5.1 Procedure for modal analysis in *MSC Adams*

In *MSC Adams*, it is possible to perform a modal analysis of the full model and thereby compute its natural frequencies and mode shapes. This is done by means of the *EIGENSOL* command, which computes the eigenvalues and eigenvectors of the linearized system.

The procedure followed to perform the modal analysis can be summarized in four main steps:

1. simulation of the system up to the operating point of interest;
2. linearization of the system equations of motion;
3. computation of eigenvalues and eigenvectors;
4. post-processing of the results.

In the present work, scripted simulations in *MSC Adams* were used. Therefore, a simulation script had to be defined before launching the analysis. Figure 5.1

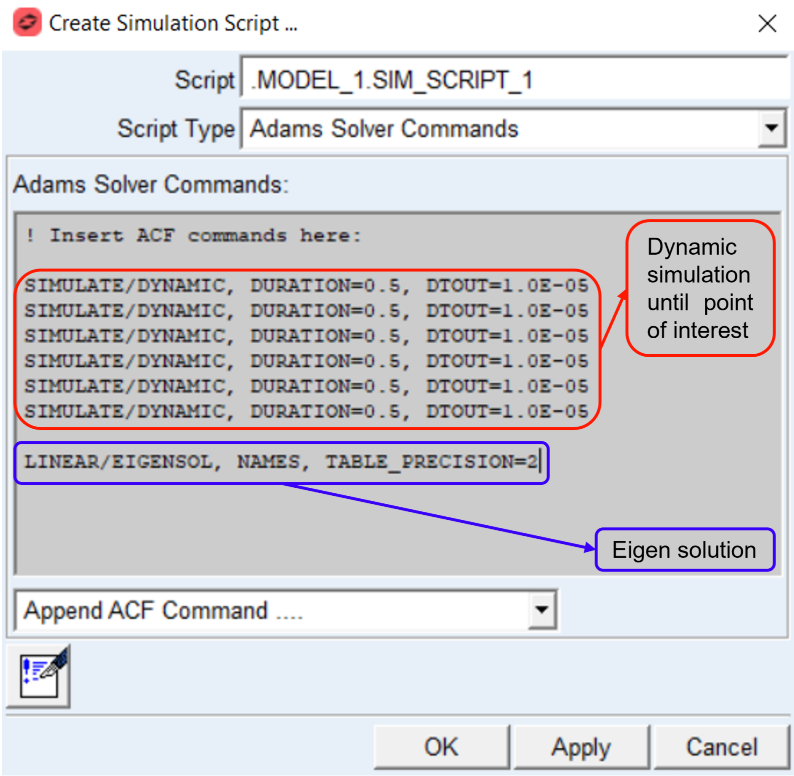

Figure 5.1: Simulation script window showing the implementation in *MSC Adams* of the steps required to perform the modal analysis.

shows the script implementing the first three steps of the modal-analysis procedure. The initial commands are used to simulate the model up to the operating point of interest. As can be seen, time-interval partitioning is also implemented, as discussed in subsection 3.3.2. The final command corresponds to the execution of the *eigen solution*.

Simulating the model up to the operating point of interest is necessary because the modal solution depends on the system condition at the time of linearization. The computed natural frequencies were found to vary, in some cases significantly, when the *eigen solution* was evaluated at different simulation times. Moreover, performing the *eigen solution* without first simulating the system led to markedly different results. A possible explanation is that, at the beginning of the simulation, the gear contacts are not yet fully established and the system has not yet reached its steady operating condition. This may affect the forces exchanged among the gears and, more generally, the overall stress state of the system, thereby influencing the computed natural frequencies. However, this interpretation should be regarded as a plausible hypothesis rather than a demonstrated conclusion.

The second and third steps are carried out automatically by the software when the *eigen solution* is executed. After execution, the results can be post-processed by examining the computed eigenvalues in tabular form, including their real part and associated frequency, and by visualizing the corresponding mode shapes through animation. The window associated with the *EIGENSOL* command is shown in Figure 5.2.

First, the software computes the state matrix of the system by directly linearizing the equations of motion. These equations are constructed using the state variables,

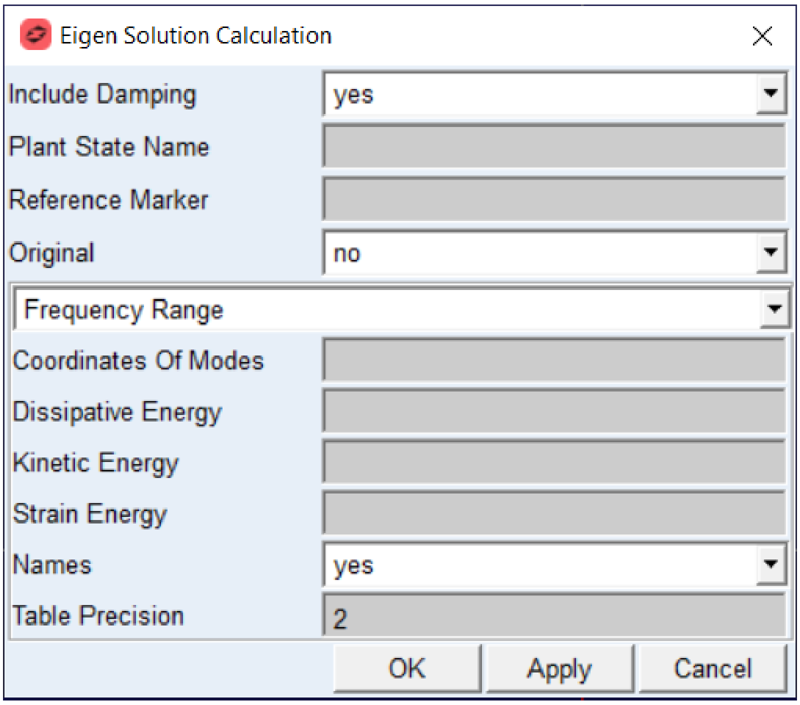

Figure 5.2: *Eigen solution* calculation window in *MSC Adams*.

which are selected from the default coordinates of the model.

According to the solver documentation, in the presence of rotating components it may be preferable to use relative coordinates. To this end, the *Reference Marker* (*RM*) option can be used. This option allows the user to define a marker to be adopted by the software as the reference frame for the automatic selection of the state variables. If the selected *RM* is body-fixed, the state variables selected by the software are expressed in a relative coordinate system.

Alternatively, the user may directly specify the state variables to be used in the equations of motion. In this case, a *PSTATE* (*Plant State*) variable must be created. To define the equations of motion, the number of selected state variables must be equal to the number of degrees of freedom of the system. If too few state variables are selected, *MSC Adams* automatically selects the remaining ones. Conversely, if too many variables are selected, the software automatically discards the redundant ones. A detailed example involving *PSTATE* is reported in Appendix B.

If both an *RM* and a *PSTATE* are defined, *MSC Adams* assigns higher priority to the user-defined states specified by the variables referenced in the *PSTATE* object, whereas the default coordinates generated through the *RM* option are assigned lower priority. Moreover, in the presence of nonlinearities in the analyzed system, different choices of *RM* or *PSTATE* may lead to different computed natural frequencies.

The information presented above, together with a more in-depth discussion, can be found in *Welcome to the C++ version of Adams Solver* > *C++ commands* > *Linear* > *Eigensolutions* in the Adams Solver User's Guide [6].

5.2 Variation of natural frequencies during the simulation

In this section, the variation of the natural frequencies over time is discussed.

At the beginning of this work, only a limited number of *eigen solutions* were evaluated at selected simulation times. The results of this preliminary analysis suggested that the natural frequencies could vary considerably, without exhibiting a clearly recognizable pattern.

The next step was therefore to examine this behavior over a shorter time interval with a finer temporal resolution. To this end, a large number of *EIGENSOL* evaluations were performed (approximately 1400). After selecting an operating angular speed, the time interval between two consecutive evaluations, Δt, was defined so that the sun gear advanced by one quarter of its pitch angle between successive evaluations. The overall time interval covered by the sequence was chosen so as to include one full revolution of the slowest component, namely the ring gear.

Figure 5.3 shows the variation over time of the natural frequencies associated with the first six mode shapes, organized into two individual modes and two complex-conjugate pairs.

Since the corresponding mode shapes cannot be shown, a brief textual description is provided to support the interpretation of the observed trends.

Modes 1.1 and 1.2. These two mode shapes are identified as a complex-conjugate pair and appear to involve the entire system. They are mainly associated with bending of the input shaft, with the end connected to the sun gear rotating counterclockwise in Mode 1.1 and clockwise in Mode 1.2. The ring gear also appears to participate through a precession motion in the same direction as the sun gear, while the planet gears appear to be involved through a radial deformation.

Mode 2. This mode is treated as an individual mode and appears to be associated only with torsion of the input shaft.

Mode 3. This mode is also treated as an individual mode and appears to involve only axial deformation of the ring gear.

Modes 4.1 and 4.2. These two mode shapes are identified as a second complex-conjugate pair and appear to involve all the gears. They appear to be similar in character to Modes 1.1 and 1.2, with the additional feature that the planet gears also exhibit a precession motion in the same direction as the sun and ring gears.

As can be seen, with the exception of Mode 3, the computed natural frequencies exhibit an oscillatory variation about a mean value over the analyzed time interval. The approximately constant behavior observed for Mode 3 is consistent with its mode shape, which appears to involve only the axial deformation of the ring gear and no rotational modal component. This interpretation is also consistent with the use of spur gears in the present system, for which the axial direction can reasonably be expected to remain largely decoupled from the in-plane motion. For this reason, Mode 3 may be regarded as a predominantly axial mode. Its nearly constant behavior may therefore be related to the fact that the periodic variations in the forces exchanged among the gears are expected to affect primarily those mode shapes involving in-plane motion, while exerting a weaker influence on a predominantly axial mode.

To further investigate these oscillatory trends, a Fast Fourier Transform was applied to the signals by means of the *fft* function in *MATLAB*, in order to identify

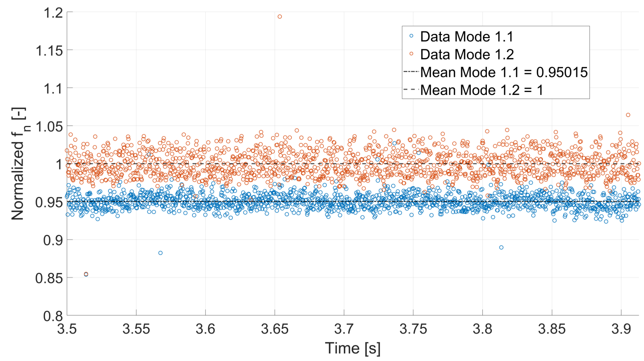

(a) Modes 1.1 and 1.2

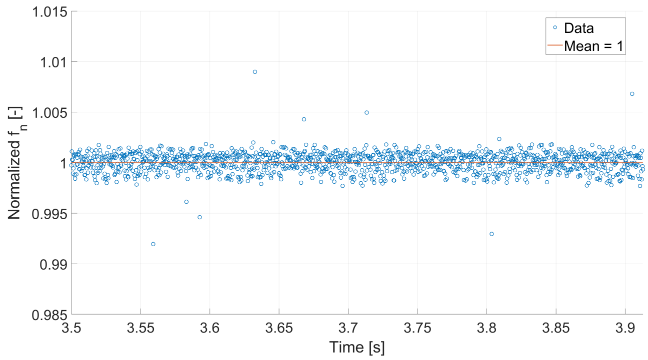

(b) Mode 2

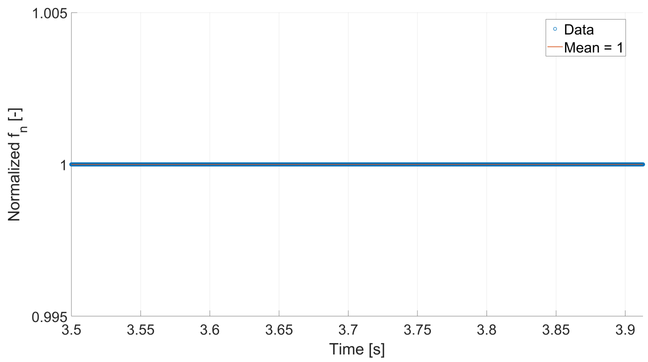

(c) Mode 3

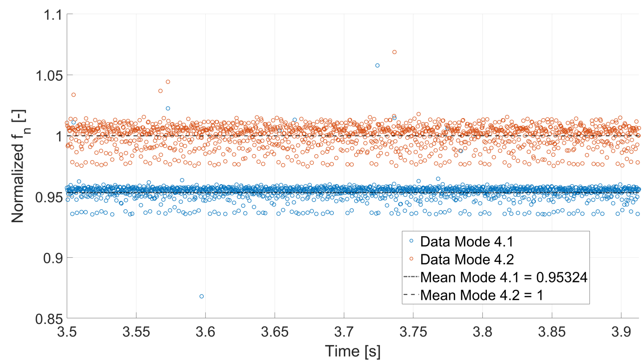

(d) Modes 4.1 and 4.2

Figure 5.3: Variation over time of the natural frequencies associated with the first six mode shapes, including two individual modes and two complex-conjugate pairs.

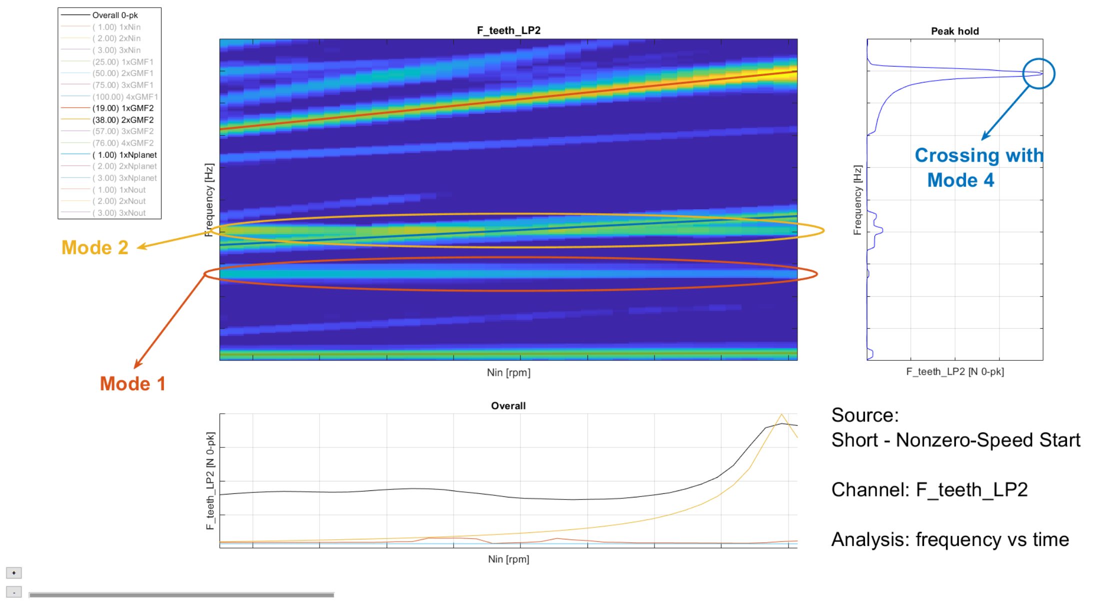

Figure 5.4: Extended Campbell diagram, including the peak-hold spectrum and overall response, used to support qualitative mode identification.

their dominant frequency components. However, for most of them, this analysis did not reveal a clear one-to-one correspondence with the relevant dynamic excitation sources of the system.

These observations also suggest that performing the *eigen solution* only once during the analysis may lead to significant errors. A plausible explanation is the presence of spurious values lying far from the mean value. For this reason, when performing modal analysis in *MSC Adams*, it is advisable to execute the *EIGENSOL* command multiple times and compute a reference mean value, preferably excluding the values lying outside a predefined admissible range.

Although the correspondence is not strictly one-to-one, some of the natural frequencies identified through the modal analysis can also be recognized, at least qualitatively, in the extended Campbell diagram shown in Figure 5.4.

In particular, the modal traces in the frequency range associated with the Mode 1 pair, namely Modes 1.1 and 1.2, and in the range associated with Mode 2 are immediately visible, whereas others are less evident and require a more detailed inspection of the diagram. The peak-hold spectrum also exhibits its maximum peak in a frequency range consistent with the Mode 4 pair, namely Modes 4.1 and 4.2. Despite the limitations discussed above, the modal-analysis procedure presented in this chapter provides useful complementary information, since it makes it possible to associate specific mode shapes with the observed traces. This, in turn, supports the identification and interpretation of the modal traces appearing in the Campbell diagram.

5.3 Parameters affecting natural frequencies

This section briefly discusses some of the parameters that may affect the computed natural frequencies.

The parameters considered are the input-shaft speed, the resisting torque applied to the ring gear, and the use of a body-fixed *Reference Marker* (*RM*) instead of the default inertial one. Several tests were performed by varying these parameters. In particular, for the input-shaft speed, in addition to the baseline simulation, two further analyses were carried out at 4x and 6x the baseline speed. For the resisting torque, an additional analysis was performed at 1.5x the baseline value.

Some tests were also carried out to assess the effect of the *Reference Marker*. However, the results were found to depend markedly on the selected reference marker. In particular, when a marker located at the input-shaft hinge was used, differences were observed in the complex-conjugate pairs, with an increased frequency separation between the two modes of each pair. By contrast, the individual modes did not show significant changes. When a *RM* located on the ring gear was used instead, the results were found to be very similar to those obtained in the baseline inertial case.

Since no clear explanation was identified for the differences observed among the tested cases, the corresponding results are not reported in this thesis and are mentioned here only qualitatively. Nevertheless, the tests performed indicate that the choice of *Reference Marker* affects the computed natural frequencies. This is consistent with the fact that the use of a *Reference Marker* changes the state variables automatically selected by the solver for the formulation and linearization of the equations of motion. In a nonlinear system such as the one considered here, this may lead to differences in the computed results, although the way in which these differences develop could not be clearly established in the present work.

The next subsections compare the modal analyses performed on the same model under different input-shaft speeds and resisting torques applied to the ring gear.

5.3.1 Effect of speed

This subsection discusses the effect of the input-shaft speed on the computed natural frequencies.

In addition to the baseline simulation, two further analyses were carried out with input-shaft speeds equal to 4 and 6 times the baseline value. All the other analysis parameters were kept unchanged, including the number of *EIGENSOL* evaluations and the time interval Δt between consecutive solutions.

A limited sensitivity to speed variation was initially expected. This expectation was mainly based on the fact that gyroscopic effects are not included in the present model; if they were, a more pronounced dependence of the computed natural frequencies on rotational speed would generally be expected. In addition, the use of an inertial reference frame suggested that no further variation of the computed natural frequencies would arise from frame-related effects of this type.

Figure 5.5 shows the effect of the input-shaft speed on the computed natural frequencies.

The plotted quantities represent the normalized evolution of the first six natural frequencies obtained from repeated *eigen solutions* of the multibody model. At each evaluation, the first six frequencies were extracted and grouped according to their modal nature, with the first and fourth modal families treated as complex-conjugate pairs. A common normalization was adopted using the baseline simulation as reference. More specifically, the normalization factors were defined from the fil-

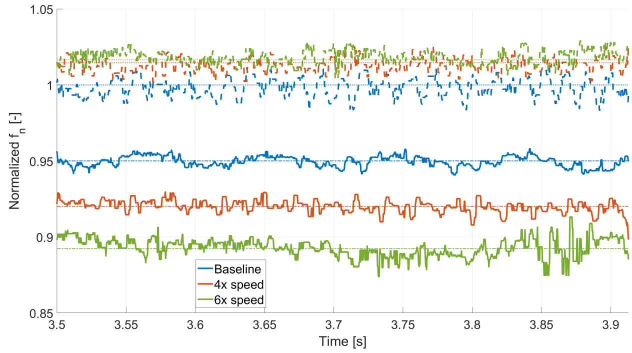

(a) Modes 1.1 and 1.2

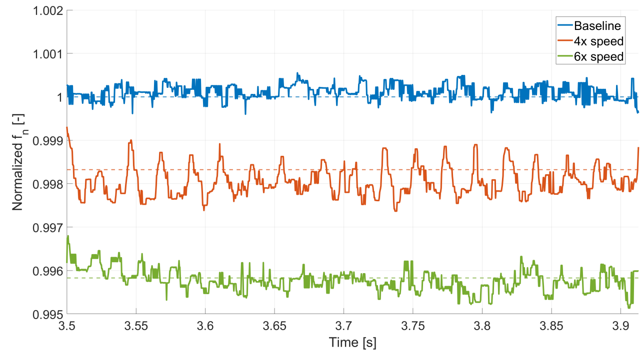

(b) Mode 2

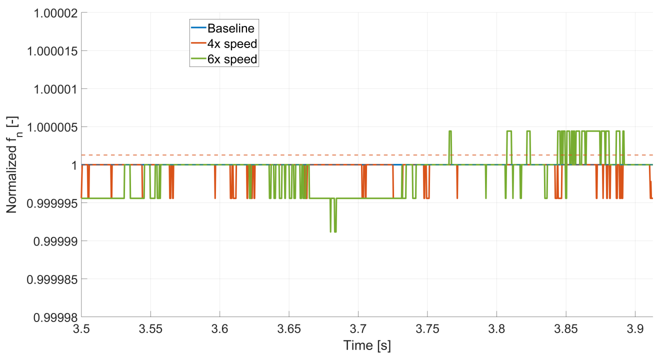

(c) Mode 3

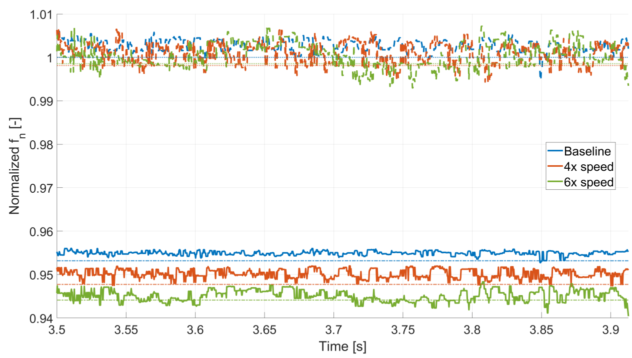

(d) Modes 4.1 and 4.2

Figure 5.5: Effect of input-shaft speed on the computed natural frequencies, shown as normalized frequency histories smoothed using *movmedian*.

tered mean frequency values of the baseline case, computed after discarding spurious points outside predefined acceptance intervals. To obtain a clearer representation of the temporal trends and reduce the influence of outliers, the raw frequency histories were smoothed by means of the *movmedian* function in *MATLAB* [10]. The filtered mean values are also reported in the plots to enable a direct comparison among the different cases.

As shown in Figure 5.5, the effect of speed depends on the mode considered.

Modes 1.1 and 1.2. These two modes exhibit an increasing separation as the input-shaft speed increases. In the first plot, they are distinguished by line style, with a solid line for *Mode 1.1* and a dashed line for *Mode 1.2*.

Mode 2. This mode is only slightly affected by speed variation. As the input-shaft speed increases, its natural frequency oscillates about a slightly lower level.

Mode 3. This is the least affected mode. No significant variation in its mean value can be observed as the input-shaft speed changes. The main visible difference is that, at higher speed, the signal appears to oscillate more markedly. This result is consistent with the physical nature of the mode, which is associated exclusively with the axial deformation of the ring gear. A weak dependence on the rotational speed is therefore to be expected.

Modes 4.1 and 4.2. Both modes show a decrease in mean natural frequency as the input-shaft speed increases. However, this effect is more pronounced for *Mode 4.1* than for *Mode 4.2*.

Overall, no general trend common to all the natural frequencies can be identified as the input-shaft speed varies, since the response depends on the specific mode under consideration. The results therefore suggest that the expected weak speed dependence is only partially reflected in the computed response. A separate observation concerns the oscillatory content of the frequency histories. This behavior cannot be directly inferred from the plots reported in Figure 5.5, as the displayed curves were intentionally smoothed to improve readability. Nevertheless, additional inspection of the raw frequency histories suggests that the oscillation frequency about the mean value may scale with the input-shaft speed. In an additional test, not reported here, in which the baseline speed was halved, the first identifiable oscillation frequency also appeared to be approximately halved. In the higher-speed cases, this feature could not be recognized as clearly by visual inspection, since the signal exhibits a much denser oscillatory pattern.

5.3.2 Effect of resisting torque

This subsection discusses the effect of the resisting torque applied to the ring gear on the computed natural frequencies.

In addition to the baseline simulation, a further analysis was carried out with a resisting torque equal to 1.5 times the baseline value. As in the previous study, all the other analysis parameters were kept unchanged, including the number of *EIGENSOL* evaluations and the time interval Δt between consecutive solutions.

A variation of the computed natural frequencies with resisting torque was expected from the outset. In particular, a more evident sensitivity was expected for those modes involving in-plane deformation, since the applied torque affects the gear-mesh stiffness through Hertzian contact and tooth bending. By contrast, a weaker dependence was expected for modes with a predominantly axial character.

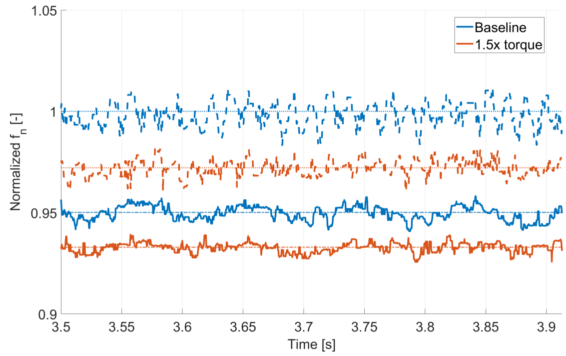

(a) Modes 1.1 and 1.2

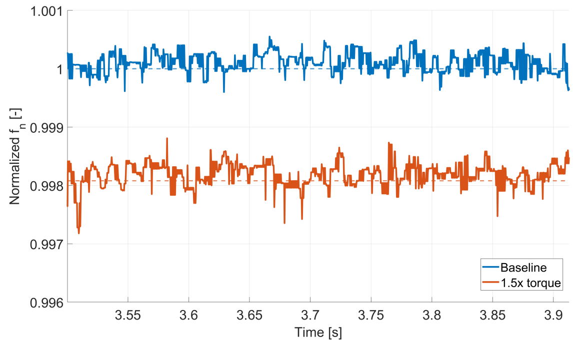

(b) Mode 2

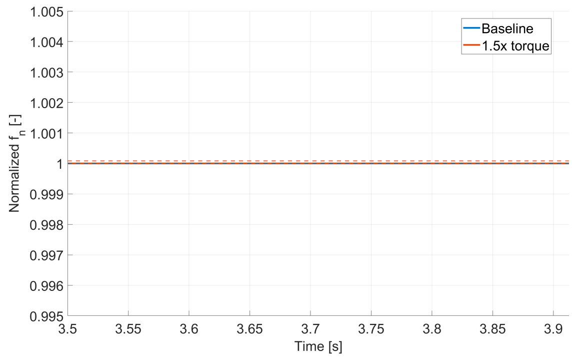

(c) Mode 3

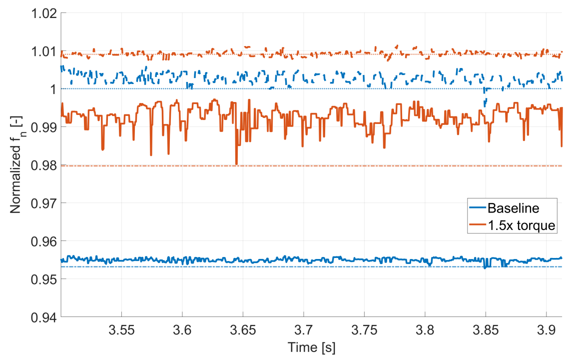

(d) Modes 4.1 and 4.2

Figure 5.6: Effect of ring-gear resisting torque on the computed natural frequencies, shown as normalized frequency histories smoothed using *movmedian*.

Figure 5.6 shows the effect of the resisting torque applied to the ring gear on the computed natural frequencies.

As in the previous case, the plotted quantities represent the normalized time evolution of the first six natural frequencies obtained from repeated *eigen solutions* of the multibody model. The normalization factors were defined from the mean values of the natural frequencies in the baseline simulation, computed after discarding spurious values outside predefined acceptance intervals. To improve the readability of the plots, the temporal trends were smoothed by means of the *movmedian* function in *MATLAB* [10].

As shown in Figure 5.6, the effect of the resisting torque depends on the mode considered, which is broadly consistent with the expected sensitivity of the in-plane modes to torque variation.

Modes 1.1 and 1.2. Both modes show a decrease in mean value when the resisting torque is increased.

Mode 2. Similarly to the first modal pair, this mode also exhibits a decrease in mean natural frequency as the resisting torque increases.

Mode 3. As in the case of speed variation, this is the least sensitive mode. This behavior is consistent with the physical nature of the mode, which is associated exclusively with the axial deformation of the ring gear. Since this mode does not primarily involve in-plane deformation or gear-mesh stiffness, a weak dependence on the resisting torque is expected.

Modes 4.1 and 4.2. By contrast, both modes exhibit an increase in mean natural frequency as the resisting torque increases. Furthermore, the separation between their mean values appears to decrease.

Overall, as in the previous case, no general trend common to all the natural frequencies can be identified as the resisting torque applied to the ring gear varies, since the response remains mode-dependent. However, unlike speed variation, torque variation appears to mainly affect the mean value of the computed natural frequencies, while no clear modification of the oscillatory content of the signals can be observed. This behavior is broadly consistent with the initial expectation that resisting torque would primarily influence those modes more directly associated with in-plane deformation and gear-mesh stiffness. In this respect, the resisting torque appears to mainly affect the mean level of the computed natural frequencies, with a more limited influence on their oscillatory behavior.

Chapter 6

Conclusions

This thesis investigated the dynamic and modal behavior of a reduction gearbox through a multibody model developed in *MSC Adams* using a *Gear AT*-based workflow. Overall, the work met its main objectives by improving the understanding of the software capabilities and limitations in both system-level modal analyses and dynamic simulations involving flexible bodies and high-frequency phenomena.

The results showed that the dynamic response of the model is sensitive to the selected simulation settings. In particular, shorter analyses, upward sweeps, and finer time-interval partitioning were generally associated with more physically consistent results and reduced vertical banding.

Overall, the analyses carried out on the numerical results indicated a broad consistency with the corresponding theoretical trends. At the same time, they highlighted some limitations of the adopted *HHT-I3* solver, particularly in the velocity and acceleration signals, which were affected by noise and spurious peaks. The results also suggested that the model preserves symmetry in its mean response, whereas the oscillatory component does not exhibit the same degree of symmetry. In addition, the stronger vertical banding observed after modifying only the boundary conditions supports the interpretation of this phenomenon as numerical in nature, although its exact origin remains unresolved.

The modal-analysis activities showed that the computed natural frequencies generally oscillate about a reference mean value and may include isolated outliers, so that a single *eigen solution* may not be representative of the system behavior at a given operating condition. The analyses also indicated that the effects of input-shaft speed and ring-gear resisting torque on the computed natural frequencies are mode-dependent, with no single general trend across all the analyzed modes. Moreover, the choice of *Reference Marker* was found to affect the computed results, although its influence could not be fully characterized within the scope of the present work. Despite these limitations, the modal-analysis procedure still provided useful complementary information, since it supported the qualitative identification of modal traces in the extended Campbell diagram and their interpretation through the associated mode shapes.

Taken together, these results suggest that *MSC Adams* provides useful capabilities for the dynamic simulation of the modeled reduction gearbox, especially with respect to the consistency of the mean response. However, numerical artifacts such as vertical banding can introduce spurious peaks and noise into the simulation results, thereby limiting the robustness of the obtained response under some operating conditions.

With regard to modal analysis, the results suggest a more limited suitability of the adopted workflow for the present application. In particular, the need to simulate the model up to the operating point of interest can make the procedure computationally expensive. In addition, the need to compute multiple *eigen solutions*, because of the oscillatory behavior of the natural frequencies, further increases the computational effort and complicates the interpretation of the results.

Several possible developments can be identified for future work. Regarding the dynamic simulations, it would be worthwhile to test higher-order solvers, such as *GSTIFF-SI2*, to assess possible noise reductions, especially in the angular-velocity and angular-acceleration datasets. Further model refinement could also be considered in order to obtain a more representative system and potentially improve the results. One possible step in this direction would be to replace the ideal hinges used in the current model with elements characterized by finite stiffness. In addition, a more detailed investigation of the contact parameters in the *Gear AT Force* settings could help reduce some of the rigid-body oscillations observed in the model.

Regarding modal analysis, future work could focus on clarifying the effect of the *Reference Marker* on the computed natural frequencies. Another potentially relevant step would be to investigate the possibility of saving and exporting the model state after the initial dynamic simulation. Although this option is described in the software documentation, it was not explored in the present work. If feasible, it could make it possible to preserve the flexible state reached after the initial transient and at a predefined operating point. This could reduce the computational time of the overall analysis by allowing the series of *eigen solutions* to be computed without repeating the initial simulation phase.

Appendix A

Derivation of the Theoretical Reference Quantities

This appendix presents the theoretical relations used to derive the results discussed in section 4.2.

In the considered configuration, the motion is applied to the input shaft, to which the sun gear is connected. A constant angular acceleration is imposed, and the system starts from standstill. The counterclockwise rotation of the sun gear is taken as positive. The adopted subscripts are listed in Table A.1.

A.1 Angular positions

Neglecting shaft flexibility, the angular position of the sun gear is

$$\theta_s(t) = \frac{1}{2}\alpha_s t^2$$

where α_s is the imposed sun gear angular acceleration and t is the simulation time.

The angular positions of the other gears are obtained from the transmission ratios:

$$\theta_{LP}(t) = -\frac{Z_s}{Z_{LP}}\theta_s(t)$$

$$\theta_{SP}(t) = \theta_{LP}(t)$$

$$\theta_r(t) = \frac{Z_{SP}}{Z_r}\theta_{SP}(t)$$

Subscript	Component
s	sun gear
LP	large planet gear
SP	small planet gear
r	ring gear

Table A.1: Definition of the subscripts used in the theoretical model.

where Z_s, Z_{LP}, Z_{SP}, and Z_r are the numbers of teeth of the corresponding gears.

A.2 Angular velocities

Since the angular acceleration is constant, the angular velocities vary linearly with time. For the sun gear,

$$\omega_s(t) = \alpha_s t$$

The remaining angular velocities are

$$\omega_{SP}(t) = \omega_{LP}(t) = -\frac{Z_s}{Z_{LP}}\omega_s(t)$$

$$\omega_r(t) = \frac{Z_{SP}}{Z_r}\omega_{SP}(t)$$

For the present speed-reduction gearbox, the angular velocity magnitudes satisfy

$$|\omega_r(t)| < |\omega_{SP}(t)| = |\omega_{LP}(t)| < |\omega_s(t)|$$

with $Z_{LP} > Z_s$ and $Z_r > Z_{SP}$.

A.3 Angular accelerations

The angular accelerations are constant. For the sun gear, the angular acceleration coincides with that imposed at the input shaft. The remaining angular accelerations are

$$\alpha_{SP} = \alpha_{LP} = -\frac{Z_s}{Z_{LP}}\alpha_s, \qquad \alpha_r = \frac{Z_{SP}}{Z_r}\alpha_{SP}$$

A.4 Transmitted torque

For the transmitted torques, the same sign convention adopted for the rotational quantities is used.

Starting from the ring gear, the torque balance can be written as

$$T_{\text{prop}} - T_r = J_r\alpha_r \qquad \Rightarrow \qquad T_r = T_{\text{prop}} - J_r\alpha_r$$

where T_{prop} is the torque applied by the inertia of the propeller and output shaft, T_r is the torque associated with the ring gear, J_r is the polar mass moment of inertia of the ring gear, and α_r is its angular acceleration.

Assuming symmetric load sharing among the three small planet gears,

$$T_{SP} = \frac{T_r}{3}\frac{Z_{SP}}{Z_r}$$

Under the rigid-body assumption,

$$T_{LP} = T_{SP}, \qquad T_s = -3\,T_{LP}\,\frac{Z_s}{Z_{LP}}$$

Appendix B

Example of state-variable selection using *PSTATE*

This appendix presents an example of the use of the *PSTATE* option to select the user-defined state variables adopted in the formulation of the equations of motion. The example is based on the case presented in [11], whereas the derivation of the equations of motion and of the corresponding eigenvalues is developed here for completeness. The appendix also shows how a different choice of state variables may affect the computed eigenvalues and, consequently, the natural frequencies of the system.

The example is based on the simplified model of a helicopter blade shown in Figure B.1. The model consists of a driving link rotating about the fixed point O according to the prescribed angular law

$$\theta(t) = wt,$$

and a rigid blade hinged at point H, located at a distance e from the rotation axis. The center of mass G of the blade is located at a distance l from the hinge, the blade mass is m, and its mass moment of inertia about its center of mass is I.

This system has only one degree of freedom; therefore, only one state variable is required to write the equation of motion. In the following sections, the derivation of the equation of motion is presented for two different choices of state variable:

1. the absolute angular coordinate α of the blade with respect to the horizontal direction;

2. the vertical coordinate y of the center of mass of the blade.

B.1 Formulation in Terms of the Absolute Angular Coordinate α

In the present formulation, the generalized coordinate is chosen as the absolute blade angle with respect to the inertial reference frame,

$$\alpha = \alpha(t).$$

Accordingly, the relative angle between the blade and the driving link is

$$\alpha - \theta = \alpha - wt.$$

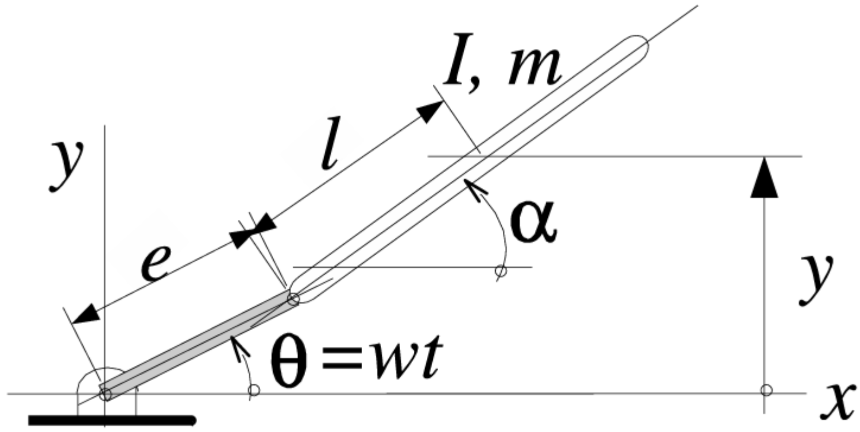

Figure B.1: Simplified model of a helicopter blade.

B.1.1 Position and velocity of the center of mass

The position of the blade center of mass is

$$x_G = e\cos(wt) + l\cos\alpha, \qquad y_G = e\sin(wt) + l\sin\alpha.$$

Differentiating with respect to time yields

$$\dot{x}_G = -ew\sin(wt) - l\dot{\alpha}\sin\alpha, \qquad \dot{y}_G = ew\cos(wt) + l\dot{\alpha}\cos\alpha.$$

Hence, the squared speed of the center of mass is

$$v_G^2 = \dot{x}_G^2 + \dot{y}_G^2.$$

Substituting the previous expressions, expanding the result, and using the trigonometric identities

$$\sin^2\beta + \cos^2\beta = 1, \qquad \sin A\sin B + \cos A\cos B = \cos(A - B),$$

one obtains

$$v_G^2 = e^2w^2 + l^2\dot{\alpha}^2 + 2el\,w\dot{\alpha}\cos(\alpha - wt).$$

B.1.2 Kinetic energy and equation of motion

The total kinetic energy of the blade is the sum of the translational kinetic energy of its center of mass and the rotational kinetic energy about its center of mass:

$$E_k = \frac{1}{2}mv_G^2 + \frac{1}{2}I\dot{\alpha}^2.$$

Substituting the expression for v_G^2 and rearranging yields

$$E_k = \frac{1}{2}(I + ml^2)\dot{\alpha}^2 + mel\,w\dot{\alpha}\cos(\alpha - wt) + \frac{1}{2}me^2w^2.$$

No potential energy contribution is considered in the present model; therefore,

$$E_p = 0, \qquad L = E_k.$$

Lagrange's equation associated with the generalized coordinate α can then be written as

$$\frac{d}{dt}\left(\frac{\partial E_k}{\partial \dot\alpha}\right) - \frac{\partial E_k}{\partial \alpha} = 0.$$

The required derivatives are

$$\frac{\partial E_k}{\partial \dot\alpha} = (I + ml^2)\dot\alpha + mel\,w\cos(\alpha - wt),$$

$$\frac{d}{dt}\left(\frac{\partial E_k}{\partial \dot\alpha}\right) = (I + ml^2)\ddot\alpha - mel\,w\sin(\alpha - wt)(\dot\alpha - w),$$

and

$$\frac{\partial E_k}{\partial \alpha} = -\,mel\,w\dot\alpha\sin(\alpha - wt).$$

Substituting these expressions into Lagrange's equation and simplifying yields the nonlinear equation of motion:

$$\boxed{(I + ml^2)\ddot\alpha + mel\,w^2\sin(\alpha - wt) = 0}$$

B.1.3 Linearization and eigenvalues

To linearize the equation, it is convenient to introduce the relative angular displacement

$$\delta = \alpha - wt.$$

Since w is constant,

$$\dot\delta = \dot\alpha - w, \qquad \ddot\delta = \ddot\alpha.$$

Accordingly, the nonlinear equation of motion becomes

$$(I + ml^2)\ddot\delta + mel\,w^2\sin\delta = 0.$$

Assuming small oscillations about the nominal configuration $\delta = 0$, the approximation

$$\sin\delta \approx \delta$$

can be used, so that the linearized equation becomes

$$\boxed{\ddot\delta + \frac{mel\,w^2}{I + ml^2}\,\delta = 0}$$

The eigenvalues are obtained by assuming a solution of the form

$$\delta(t) = e^{\lambda t}.$$

Substituting into the linearized equation yields

$$(I + ml^2)\lambda^2 + mel\,w^2 = 0.$$

Therefore, the eigenvalues are

$$\boxed{\lambda_{1,2} = \pm i\,w\sqrt{\frac{mel}{I + ml^2}}} \qquad \text{(B.1)}$$

B.2 Formulation in Terms of the Vertical Coordinate y

An alternative linearized formulation may be obtained by expressing the dynamics in terms of the vertical coordinate of the blade center of mass. Instead of repeating the full derivation from scratch, the procedure starts from the linearized equation in the relative angular displacement δ,

$$\ddot{\delta} + \frac{mel\,w^2}{I + ml^2}\,\delta = 0.$$

B.2.1 Kinematic relation between y and δ

The vertical coordinate of the center of mass is

$$y = e\sin(wt) + l\sin\alpha.$$

Since

$$\alpha = wt + \delta,$$

one obtains

$$y = e\sin(wt) + l\sin(wt + \delta).$$

Assuming δ to be small, the first-order Taylor approximation

$$\sin(wt + \delta) \approx \sin(wt) + \delta\cos(wt)$$

can be used, giving

$$y \approx (e + l)\sin(wt) + l\cos(wt)\delta.$$

Differentiating with respect to time yields

$$\dot{y} \approx (e + l)w\cos(wt) - lw\sin(wt)\delta + l\cos(wt)\dot{\delta}.$$

Differentiating once more yields

$$\ddot{y} \approx -(e + l)w^2\sin(wt) - lw^2\cos(wt)\delta - 2lw\sin(wt)\dot{\delta} + l\cos(wt)\ddot{\delta}.$$

The linearization is performed about the operating point

$$t = 0, \qquad \delta = 0, \qquad \dot{\delta} = 0,$$

which corresponds to

$$\alpha = 0, \qquad \dot{\alpha} = w.$$

At $t = 0$, the previous relations reduce to

$$y \approx l\delta,$$
$$\dot{y} \approx (e + l)w + l\dot{\delta},$$
$$\ddot{y} \approx -lw^2\delta + l\ddot{\delta}.$$

Using the approximation $y \approx l\delta$, the last expression may be rewritten as

$$\ddot{y} = l\ddot{\delta} - w^2 y,$$

that is,

$$\ddot{\delta} = \frac{\ddot{y} + w^2 y}{l}.$$

Moreover,

$$\delta \approx \frac{y}{l}.$$

B.2.2 Linearized equation in y and eigenvalues

Substituting

$$\ddot{\delta} = \frac{\ddot{y} + w^2 y}{l}, \qquad \delta = \frac{y}{l}$$

into the linearized equation in δ yields the linearized equation of motion in terms of the vertical coordinate:

$$\boxed{\ddot{y} + w^2 \left(1 + \frac{mel}{I + ml^2}\right) y = 0}$$

The eigenvalues are again obtained by assuming a solution of the form

$$y(t) = e^{\lambda t}.$$

Substituting into the linearized equation yields

$$\lambda^2 + \left(w^2 + \frac{mel\, w^2}{I + ml^2}\right) = 0.$$

Therefore, the eigenvalues are

$$\boxed{\lambda_{1,2} = \pm i\, w \sqrt{1 + \frac{mel}{I + ml^2}}} \qquad \text{(B.2)}$$

B.3 Comparison of the computed eigenvalues

As shown by the previous derivations, using two different state variables to write the equation of motion leads to different expressions for the corresponding eigenvalues.

As a numerical example, the values reported in Table B.1 are used.

Quantity	Value	Unit
m	3	kg
I	10	kg m^2
e	2	m
l	10	m
w	20π	rad/s

Table B.1: Numerical values used in the example model.

For these values, the eigenvalues obtained from Equation B.1 and Equation B.2, together with the corresponding natural frequencies, are:

1. absolute angular coordinate α: $\lambda = \pm 4.3994\, i$ rad/s, corresponding to $f_n = 0.7002$ Hz;

2. vertical coordinate y: $\lambda = \pm 10.9250\, i$ rad/s, corresponding to $f_n = 1.7388$ Hz.

Figure B.2: *Adams* representation of the helicopter blade model and relevant markers.

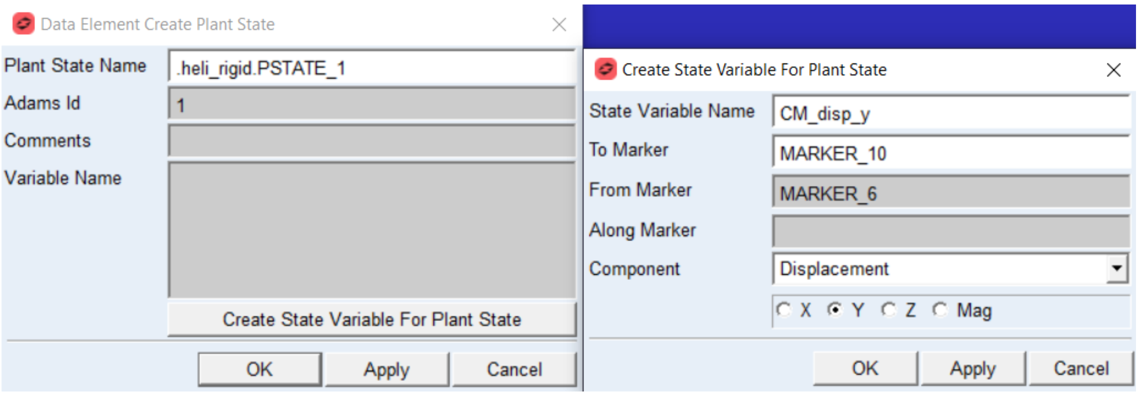

Figure B.3: Creation of a *PSTATE* and definition of the associated state variable in *Adams*.

As can be seen, linearizing the same system using two different state variables leads to different computed eigenvalues and, consequently, to different natural frequencies. This difference does not arise from different physical effects in the system, but from the fact that linearization is a local approximation of the original nonlinear equations of motion. As a result, different choices of state variables lead to different linearized forms of the same system and, consequently, to different eigenvalues. The stronger the nonlinear character of the system, the more pronounced this effect may become.

Since the system analyzed in this thesis contains several nonlinearities, a suitable choice of the state variables is required when using *PSTATE*. In systems including flexible bodies, the number of degrees of freedom may become very large. In such cases, as in the model discussed in this thesis, defining all the state variables explicitly may be impractical. Therefore, only a subset of them may be selected through *PSTATE*, while the remaining ones are automatically selected by *Adams*. Alternatively, the complete selection may be left to the software.

B.4 Implementation of *PSTATE* in *Adams*

This section presents the *Adams* model of the helicopter blade discussed above and explains how to select a specific state variable by means of the *PSTATE* option.

Figure B.2 shows the *Adams* representation of the helicopter blade model together with the absolute reference frame. In this model, if no user-defined choice is specified, the software uses the absolute angular coordinate α as the state variable.

Figure B.3 shows the windows used to define the *PSTATE* variable. To select the vertical coordinate y of the blade center of mass, a *PSTATE* must be defined as shown in the figure. Specifically, the user must define the marker to be monitored (*To Marker*), the reference marker (*From Marker*), and the quantity of interest. In the present case, the monitored marker is *MARKER_10*, which is fixed to the blade and located at its center of mass. The reference marker is *MARKER_6*, which is fixed to the ground and located at the blade hinge. The selected quantity is the displacement along the y-direction.

With this definition, the vertical displacement of the blade center of mass is used as the user-defined state variable in the linearization process

Bibliography

[1] Daniele Di Piazza. “Multibody dynamic analysis of geared transmission systems”. Developed in collaboration with Avio Aero. Master’s thesis. Politecnico di Torino, 2026.

[2] Hexagon. Adams 2024.1 Adams Machinery User’s Guide. Official online documentation. 2024.

[3] Ahmed A. Shabana. *Dynamics of multibody systems / Ahmed A. Shabana*. eng. 4th ed. New York: Cambridge University Press, 2013. ISBN: 9781107042650.

[4] Ahmed A. Shabana. *Computational Dynamics*. 3rd ed. Chichester, West Sussex, United Kingdom: John Wiley & Sons, Ltd., 2010. ISBN: 978-0-470-68615-7.

[5] Hans M. Hilber, Thomas J. R. Hughes, and Robert L. Taylor. Improved numerical dissipation for time integration algorithms in structural dynamics. In: *Earthquake Engineering & Structural Dynamics* 5.3 (1977), pp. 283–292. DOI: 10.1002/eqe.4290050306.

[6] Hexagon. Adams 2024.1 Adams Solver User’s Guide. Official online documentation. 2024.

[7] A. Kahraman and R. Singh. Non-linear dynamics of a spur gear pair. In: *Journal of Sound and Vibration* 142.1 (1990), pp. 49–75. ISSN: 0022-460X. DOI: 10.1016/0022-460X(90)90582-K.

[8] MathWorks. MATLAB Documentation: movmean. Accessed June 15, 2026. 2026.

[9] Hexagon. Adams 2024.1 Adams View User’s Guide. Official online documentation. 2024.

[10] MathWorks. MATLAB Documentation: movmedian. Accessed June 15, 2026. 2026.

[11] Hexagon SimCompanion. AS-018: Using PSTATE for Computing Eigenvalues of a Rigid Helicopter Blade. Online technical note. 2026.